Mineralogy and Petrology
https://doi.org/10.1007/s00710-025-00909-1

RESEARCH

Extent of the São Francisco Craton, South America: a mantle perspective

Nadine P. Cooper[1] · James M. Scott[1,2] · D. Graham Pearson[3] · Rogerio G. Azzone[4] · Felipe P. Leitzke[5] · S. Woodland[3] · Jose P. Donatti-Filho[6] · M. Palmer[1] · Malcolm R. Reid[1] · Andrew J. Schaeffer[7]

Received: 4 November 2024 / Accepted: 11 March 2025

Abstract
Although cratons owe their longevity to thick, depleted and consequently buoyant sub-continental lithospheric mantle, their extents are commonly indicated by the known distribution of crustal rocks. However, the limits of a mapped cratonic area often do not match the seismically imaged thick sub-continental lithospheric mantle roots. New mantle xenolith petrology and geochemistry, combined with continental scale geophysical data, confirm the interpretation that the São Francisco Craton extends beyond the extent of surface exposures of Archean rocks. Mantle xenoliths from outside the typically recognised São Francisco Craton boundaries from the Limeira-1 and Redondão kimberlite diatremes have refractory olivine [Mg# ≤ 93, with Mg# = 100× molar Mg/(Mg+Fe); Limeira], high-Cr pyrope garnets ($Cr_2O_3 \leq 7$ wt% from Redondão), low bulk $Al_2O_3 < 1$ wt%, and $^{187}Os/^{188}Os_i$ = 0.11202–0.11916 (Limeira) and 0.10964–0.11576 (Redondão) that equate to Mesoproterozoic minimum T_{RD} ages. Geothermobarometry indicates that the lithospheric thickness from which the Redondão xenolith suite was exhumed, extended to >150 km at the time of eruption, similar to the lithosphere thickness estimated from garnet pyroxenites from the 'on-craton' Braúna field. The occurrence of thick, refractory and ancient lithosphere extending outside the known surface extent of the São Francisco Craton suggests that this cratonic nucleus is significantly larger than recognised at the surface. Based on the evidence reported in this study coupled with existing literature, we propose that the current limits of the São Francisco Craton nucleus should be revised to consider deep lithosphere to the north and southwest edges, despite these areas having younger rocks at the surface.

Keywords Craton · Mantle xenolith · Peridotite · Pyroxenite · Os isotopes · São Francisco Craton

Introduction

The continent of South America has long been recognised to contain several cratonic blocks, which form long-lived portions of lithosphere that have acted as major "nuclei" during crustal growth. These cratons are typically defined in the South American literature as areas of crustal rocks older than 1.8 Ga, i.e., Paleoproterozoic or older. This perspective differs slightly from other common uses worldwide, where it is applied to Archean and earlier-formed crustal rocks (De

Editorial handling: K. Smit.

✉ Nadine P. Cooper
nadine.cooper@postgrad.otago.ac.nz

[1] Department of Geology, University of Otago, 360 Leith Street, Dunedin 9054, New Zealand

[2] Department of Geoscience, Aarhus University, Høegh-Guldbergs Gade 2, Aarhus 8000, Denmark

[3] Department of Earth and Atmospheric Sciences, University of Alberta, 1-26 ESB, Edmonton, AB T6G 2E3, Canada

[4] Instituto de Geociências, Universidade de São Paulo, R. do Lago, 562 – Butantã, São Paulo 05508-080, Brazil

[5] Geological Engineering Department, Universidade Federal de Pelotas, 10, R. Xavier Ferreira, 2 - Porto, Pelotas, RS 96010-540, Brazil

[6] Lipari Mineracao Ltda, R. João Chagas Ortins de Freitas, 517 - Jardim Talaya, Lauro de Freitas - BA 42700-000, Brasil

[7] Pacific Division, Geological Survey of Canada, Natural Resources Canada, 9860 W Saanich Rd, Sidney, BC V8L 5T5, Canada

Published online: 11 April 2025

Wit et al. 1992; Bleeker 2003). However, critical to the discussion of what comprises a craton is the recognition that the ancient crustal rocks are not the major component to the lithosphere. While it is recognised that the total extent of crustal rocks may be concealed by burial and/or erosional processes, it is the lithospheric mantle roots that comprise and define the majority of cratons (Pearson et al. 2021). These roots impart the critical long-term stability of cratons via increased buoyancy (Vandenburg et al. 2023) and strength (Cooper et al. 2006), resulting from high degrees of melting (Boyd 1989; Herzberg and Rudnick 2012). In this context, a craton should be more adequately considered as an area of thick Precambrian lithosphere that has been stable for ca. 1 Ga, i.e., it demonstrates a stability of thick lithosphere that long exceeds orogenesis (Pearson et al. 2021).

Here, we present a geochemical and petrological study of two suites of peridotitic mantle xenoliths (Redondão, Limeira) from outside the classically defined São Francisco Craton, and a suite of garnet pyroxenites from within the craton (Braúna). Rhenium-osmium isotopic data help to establish the chronology of the peridotites, and the mineralogical data enable calculation of temperatures and pressures for the analysed samples. Using the global seismic tomography model of Schaeffer and Lebedev (2013), the petrological observations are interpreted together with the deep geophysical perspective to propose a redefined extent of the São Francisco Craton.

Geological background

Overview

Archean nuclei in South America comprise a geological record extending back to the Eoarchean and constitute six classically defined cratons: Amazonian, São Luis, São Francisco, Luis Alves, Rio Apa, and Rio de La Plata (Fig. 1a) (Almeida et al. 2000; Hartmann et al. 2001; Cordani et al. 2010; Klein et al. 2015; Martins et al. 2017; Santos et al. 2020; Heller et al. 2021; Barbosa et al. 2022; Moreira et al. 2022). In detail, the Rio Apa and São Luis cratons may be part of the Amazonian Craton (Teixeira et al. 2017), and the Rio de la Plata Craton is now defined to exclude the Archean Nico Perez terrane that was accreted in the Neoproterozoic (Oyhantçabal et al. 2018), but extends further northeast beneath the Paleo-Mesozoic Paraná Basin where it was sutured with the Paranapanema block (Affonso et al. 2021). Our topic of study – the São Francisco Craton – comprises tonalite-trondhjemite-granodiorite (TTG) suites and granite-greenstone terranes that are usually divided between northern and southern portions, bounded by mobile belts associated to the Paleoproterozoic Trans-Amazonian and Neoproterozoic Pan-African-Brasiliano orogenies (Almeida 1977; Teixeira et al. 2017). Paleogeographic studies have recognised the São Francisco Craton as associated with the northern Congo Craton in Africa (e.g., Smith and Hallam 1970) prior to the opening of the Atlantic Ocean (Fig. 1b).

The southern São Francisco Craton comprises an Archean basement overlain by Paleoproterozoic clastic and chemical metasedimentary sequences of the Quadrilátero Ferrífero mining district (Farina et al. 2015) (Fig. 1c). Archean exposures in this area are granite-gneiss metamorphic complexes of medium to high grade metamorphism, partially migmatised and intruded by crustal differentiates, such as K-rich granites (Teixeira et al. 2000). Of particular importance in the southern São Francisco Craton are, for example, the Paleo to Neoarchean Campo Belo, Belo Horizonte and Bonfim metamorphic complexes and the Santa Bárbara and Bação Domes, which are mainly polyphase gneiss and migmatite TTG suites with a juvenile Nd isotopic signature. These units are tectonically juxtaposed to remnants of greenstone belts, such as the Fortaleza de Minas, Barbacena, Piumhi and Rio Paraúna, with an age range from 3.21 to 2.84 Ga and showing evidence for at least three distinct orogenic events that formed the Archean core of the southern São Francisco Craton (e.g., Campos and Carneiro 2008; Lana et al. 2013; Romano et al. 2013; Teixeira et al. 2017). During the Neoarchean, progressive continental accretion between 2.8 and 2.6 Ga, in an island-arc environment further contributed to the development of the Archean granite-greenstone terrains in the southern São Francisco Craton, including syn to post-orogenic calc-alkaline and tholeiitic magmatism (Machado et al. 1992; Engler et al. 2002; Noce et al. 2007; Goulart et al. 2013; Teixeira et al. 2017). The supracrustal volcano-sedimentary sequences as well as the TTG gneisses recorded in the southern São Francisco Craton were a stable continental mass by the end of the Neoarchean, being widely reworked and metamorphosed during the Paleoproterozoic around 2.2–1.9 Ga, related to the Trans-amazonian (Rhyacian–Orosirian) orogeny (e.g., Alkmim and Marshak 1998).

The Archean terranes in the northern São Francisco Craton comprise a series of blocks (Gavião, Serrinha, Jequié, Uauá) accreted in the Paleoproterozoic during the formation of the Itabuna-Salvador-Curaçá orogen at 2.1–2.0 Ga (Fig. 1c), which underwent metamorphism from greenschist to granulite facies (Barbosa and Sabaté 2004; Guimães et al. 2012; de Sousa et al. 2020; Terentiev and Santosh 2020). Eo–to Mesoarchean rocks have been reported from the Mundo Novo greenstone belt (3.4–3.3 Ga) and the TTG terranes comprising the Mairi Complex, Sete Voltas and Boa Vista/Mata-Verde massifs, the Riacho de Santana and Sobradinho complexes (3.7 to 3.1 Ga) recorded in different pulses of mainly felsic crust generation (Fig. 1c) (Marinho

Fig. 1 **a** Western Gondwana at 500 Ma showing major global cratons and Neoproterozoic mobile belts. Figure modified from Kuchenbecker et al. (2015). **b** Map of the South American continent showing the 6 major cratons based upon geological surface crustal data. Figure modified from Cordani et al. (2009). **c** Geological map of the São Francisco Craton with its current boundary based upon Almeida (1977). The craton is surrounded by various Neoproterozoic mobile belts and orogenies including the Sergipana Belt, Brasilia Belt, Ribeira Belt and the Araçuaí Belt which were formerly the pan-African-Brasiliano orogenies. Basement > 1.8 Ga is outlined and comprises various Paleo-Mesoarchean TTG (greenstone) belts including the Mundo Novo, Riacho de Santana greenstone belts and the Sete Voltas and Boa Vista/ Mata-Verde massifs. The three locations focussed on in this study are indicated, the Braúna Kimberlite Field (10°54'10"S 39°25'22"W), the Redondão kimberlite (9°15'23"S 45°33'05"W) and the Limeira-1 kimberlite(18°56'94"S 47°46'72"W) located within the Coromandel Kimberlite Field at the northern extent of the Alto Paranaiba Igneous Province (APIP) (orange) (APIP from Fernandes et al. 2021). Figure modified from Alkmim and Marshak (1998) and Lopes et al. (2021)

1991; Nutman et al. 1994; Martin et al. 1997; Guimãres et al. 2012; Oliveira et al. 2020). Later mostly Neoarchean (2.9–2.5 Ga) intra-crustal differentiated granitic intrusions also occur at the northern São Francisco Craton, similarly to the observed in the southern São Francisco Craton (Marinho et al. 1993; Leal et al. 2003; Cruz et al. 2012; Santos-Pinto et al. 2012).

Kimberlite localities

Present day seismic tomography of the São Francisco Craton reveals the sub-continental lithospheric mantle is approximately 150–175 km thick across most of the craton and beyond its classical limits to the north and south-west (Rocha et al. 2011, 2019a; Schaeffer and Lebedev 2013). In situ kimberlite-erupted diamond occurrences support the existence of thick cratonic lithosphere in the same regions as identified by tomographical models. Diamonds within the São Francisco Craton crustally defined limits are predominantly derived from the Brauna Kimberlite Field within the Serrinha block (Pereira et al. 2021). 'Off-craton' diamonds are primarily found to the south-west of the São Francisco Craton in the western part of Minas Gerais, notably within the Coromandel Kimberlite Field and the Romaria region (Svisero 1995; Coelho et al. 2010), the Mato Grosso region in western Brazil (Kaminsky et al. 2001) and the Fazenda Largo and Redondão kimberlites in Piauí State north of the São Francisco Craton (Kaminsky et al. 2009). Our mantle xenoliths come from the Limeira-1 kimberlite in the Alto Paranaiba Igneous Province (APIP), the diamondiferous Braúna Kimberlite Field, and the potentially diamondiferous Redondão kimberlite pipe (Fig. 1c; Table 1). Of these, only Braúna samples occur within the classically defined limits of the São Francisco Craton.

The Redondão kimberlite diatreme is located approximately 15 km southeast of Santa Filomena District, is estimated to have erupted during the Cretaceous (Svisero et al. 1977; Almeida-Filho and Castelo Branco 1992). It has an exposed surface area of ~1100 m^2 and geophysical data are interpreted to show that the funnel shaped structure extends ~2 km below the surface (Almeida-Filho and Castelo Branco 1992), where it intrudes Carboniferous to Permian sediments (Svisero et al. 1982). Diatreme material is pale green and highly brecciated and contains crustal- and mantle-derived xenoliths and various xenocrysts.

Limeira-1 (also referred to as Perdizes-04-A) (Azzone et al. 2022) is a Cretaceous-erupted kimberlite (Guarino et al. 2013) located in the Coromandel Kimberlite Field in the northern half of the APIP (Fig. 1c), intruding a sequence of Neoproterozoic metasedimentary/metavolcanic thrust- and fold systems (Fernandes et al. 2021). The Coromandel Kimberlite Field encompasses over 500 intrusions across an area of 11,600 km^2. The surface expanse of individual pipes within the field spans 0.01–3.6 km^2, where crater, diatreme and hypabyssal kimberlite facies are exposed to varying degrees (Fernandes et al. 2021). Peridotite xenoliths occur in some of the volcanic rocks (Coldebella et al. 2020; Azzone et al. 2022).

The Braúna Field is a ~17 km long NW-SE trending diamondiferous kimberlite and lamproite field consisting of 19 dikes and three pipe-shaped structures within the Bahia State (Donatti-Filho et al. 2013). Kimberlites intrude the late-Archean Nordestina granodiorite batholith, with U-Pb perovskite dating indicating emplacement at approximately

Table 1 Sample summary table

	Modal abundance (vol %)								
Sample	Ol	Opx	Cpx	Grt	Spl	Classification	Texture	Ol Mg#	Spl Cr#
LIM-1	93	0	0	0	7	dunite	coarse	92.6	70.5
LIM-2	62	38	0	0	0	harzburgite	mosaic porphyroclastic	91.3	n.d.*
LIM-3	100	0	0	0	0	dunite	coarse	92.5	n.d.
LIM-4	100	0	0	0	0	dunite	granuloblastic	92.2	n.d.
LIM-5	81	11	4	0	4	lherzolite	mosaic porphyroclastic	92.5	89.5
LIM-6	100	0	0	0	0	dunite	mosaic porphyroclastic	92.6	n.d.
LIM-7	80	0	10	0	10	lherzolite	mosaic porphyroclastic	92.7	50.4
B-2E	0	100	0	0	0	garnet websterite	coarse	n.d.	n.d.
B-4G	0	0	63	38	0	garnet websterite	coarse	n.d.	n.d.
B-5 H	0	0	86	14	0	garnet websterite	coarse	n.d.	n.d.
B-6I	5	23	23	42	7	garnet websterite	coarse	92.0	2.9
B-9 L	0	0	74	22	4	garnet websterite	coarse	n.d.	4.0
B-10 M	0	0	67	33	0	garnet websterite	coarse	n.d.	n.d.
B-11 N	0	0	22	78	0	garnet websterite	coarse	n.d.	n.d.
B-13P	0	0	43	57	0	garnet websterite	mosaic porphyroclastic	n.d.	n.d.

Note that Redondão samples are not included here because their modal abundance (by point counting) was not able to be determined because of extensive serpentinisation of olivine

LIM = Limeira-1 samples, B = Braúna samples, Ol = olivine, Opx = orthopyroxene, Cpx = clinopyroxene, Grt = garnet, Spl = spinel

640 Ma (Donatti Filho et al. 2008; 2010). Small garnet pyroxenite xenoliths were obtained from drill cores.

Methods

The xenoliths prepared for analysis were selected based on apparent freshness. Host kimberlite was removed using a diamond tipped saw blade and then samples were sanded using carborundum and washed to remove contamination. Eighteen samples were selected and either made into 30 µm thick polished thin sections or mounted in epoxy briquettes and subsequently carbon-coated at a thickness of 10 nm for analysis by a Zeiss Sigma variable pressure field emission scanning electron microscope (SEM) using an energy dispersive X-ray spectrometer (EDS) attachment. The SEM was operated with an aperture of 120 µm, a working distance of 8.5 mm and a 15 kV. Beam intensity was calibrated on pure cobalt and analyses standardised using Smithsonian microbeam standards Cr-Augite (Ca, Na, Al), olivine 444 or hypersthene (Mg, Si, Fe), Kakanui kaersutite KK1 (Ti), microcline (K), chromite (Cr) and fayalite (Mn) (Jarosewich et al. 1980).

Garnet and clinopyroxene grains were handpicked from Redondão and Braúna xenoliths and mounted in resin briquettes for in situ trace element analyses. Analyses were conducted using an Agilent 7900 quadrupole inductively coupled plasma-mass spectrometer (ICP-MS) linked to a Resonetics RESOlution 193 nm ArF excimer laser at 50–75 µm, a 10 Hz repetition rate, and an on-sample fluence of 2.5 J/cm^2. Individual analyses had 20 s gas background preceding 50 s of data collection. Collection of mass peak data took place with integration times of 10 ms per element in time-resolved mode with one point per peak. Background for raw mass peak count rates were subtracted and converted to concentrations using Iolite v.3.72 (Paton et al. 2011) and corrected for mass bias drift. Internal normalisation was achieved using Ca wt% measured by EDS and ^{43}Ca signals for both clinopyroxene and garnet. The method was calibrated against NIST SRM 610 (Jochum and Stoll 2008), which was run approximately every 10 analyses, and NIST SRM 612 glass (Jochum and Stoll 2008) and BHVO-2G (basaltic glass; Jochum et al. 2005) used for quality assurance of that calibration. The monitoring reference materials produced results within 16% (and mostly within 10%) of published values.

Samples for bulk analyses were pulverised using an agate mill. Powders of one aliquot were measured for major and trace elements by X-ray fluorescence. Major elements were measured on lithium tetraborate fused disks containing 0.4 g of powder, with the trace elements obtained on dried powders (110 °C) converted to pressed powder pellets that were made of 7.0 g rock powder and 1.4 g copolywax. Elements were measured on a PANalytical 2404 X-ray fluorescence vacuum spectrometer equipped with a 4 kW Rh super sharp X-ray tube. Loss on ignition (LOI) was calculated by weighing aliquots before and after experiencing 950 °C in an oven for one hour.

Re-Os isotopes and highly siderophile elements (Ir, Os, Pt, Pd, Re, Ru) concentrations were measured. For each sample, 1 g of agate-ground powder and a mixed PGE spike was dissolved for ~16 h at ~260 °C with a ^{185}Re, ^{190}Os, ^{191}Ir, ^{194}Pt, and ^{106}Pd mixed spike in Aqua Regia in a high-pressure asher (HPA-S, Anton Paar). All acids are of Fisher Trace Metal Grade that were further purified in Savillex Teflon cupola stills. Osmium was separated from other PGE using a $CHCl_3$ triple solvent extraction, back extracted into HBr (Cohen and Waters 1996), and then purified by microdistillation (Birck et al. 1997). Following Os extraction, aqua regia was evaporated before converting Re and the other PGEs to chloride form by drying repeatedly in HCl. Matrix separation was achieved using anion exchange chromatography (with BioRad AG1 X-8 anion exchange resin) modified from Pearson and Woodland (2000). Matrix separation was achieved using anion exchange chromatography (with BioRad AG1 X-8 anion exchange resin) modified from Pearson and Woodland (2000). Os isotopes and abundances were measured using negative thermal ionization mass spectrometry (N-TIMS) on a Thermo Fisher Triton Plus. A $Ba(OH)_2$ activator was used on all samples and standards. All samples in this study were analysed by peak hopping on a secondary electron multiplier. Mass fractionation was corrected to $^{192}Os/^{188}Os = 3.082614$. Accuracy and precision of the Os isotope analyses was assessed by analyzing a DrOsS standard at the start and end of each measurement session and comparing this to the long-term laboratory mean values of $^{187}Os/^{188}Os$ (0.16083 ± 0.00028; 2σ absolute; $n = 50$; 2σ relative = 1.8‰), which have been ascertained over several years through repeated measurements of the DrOsS standard. The mean $^{187}Os/^{188}Os$ for DrOsS standards measured in this study is identical within the stated level of precision, to the accepted value of 0.160924 ± 0.00004 (Luguet et al. 2008), hence the Os isotopic data are considered accurate at this level of precision. PGE and Re abundances were measured on a Nu Attom ICP-MS. Mass fractionation was corrected using synthetic 1 ppb PGE standards. Blank corrections are minor for Ir, Re, Ru, and Pd (5 pg/g or less). Blanks are slightly higher for Pt, typically in the order of 20 pg/g. The tomographical model upon which the xenoliths are projected is from Schaeffer and Lebedev (2013), and the reader is directed there for all details about its generation.

Results

Xenolith textures and major element compositions

The three mantle xenoliths collected from the Redondão kimberlite contain variable amounts of relatively fresh garnet; however, heavy weathering has resulted in complete serpentinization of olivine and most orthopyroxene and clinopyroxene grains (Table 1; Fig. 2a). Consequently, the inter-mineral textures and modal abundances are unclear, and olivine chemical compositions were unable to be determined. The garnets are 2–4 mm Cr-pyrope porphyroblasts, with MgO between 18.7 and 20.5 wt%, 5.3–6.8 wt% CaO and Cr_2O_3 4.3–7.0 wt% (Table 2). Garnet compositions from the Redondão peridotites are harzburgitic (G10), which plot below the graphite/diamond constraint (GDC), and lherzolitic (G9) (Grütter et al. 2004). (Fig. 3). Garnets are often surrounded by small < 100 µm reaction rims comprising subhedral grains of Al-rich spinel and clinopyroxene (Fig. 2a). Orthopyroxene typically presents as weathered porphyroblasts between 500 µm and 1 mm and is enstatite, with average Mg# 92.5, average Al_2O_3 between 1.5 and 3.4 wt%. Clinopyroxene is Cr-diopside with between 1.3 and 2.3 wt% Cr_2O_3 (Table 2).

The seven studied peridotite xenoliths from the Limeria-1 kimberlite are up to ~5 cm in length and are olivine-rich dunites with minor harzburgites and lherzolites, determined by point counting polished thin sections on a 200 × 200-point grid (Fig. 2b). Mineral textures vary from granuloblastic and mosaic porphyroclastic to coarse (classification of Harte 1977). The rocks comprise porphyroclasts of orthopyroxene (< 3 mm) set in an olivine-rich matrix (Fig. 2c) with rare clinopyroxene and spinel. The olivine Mg# varies between 91.3 and 92.7. The spinel has average Cr# [100× molar Cr/(Cr+Al)] between 50 and 90 (Table 1) and is usually present as small grains in and around pyroxenes but can be up to 500 µm in diameter in some samples. Although garnet does not occur in our samples, it has been reported in peridotites from the area by Carlson et al. (2007) and Braga et al. (2024).

Eight mantle xenoliths from the Braúna kimberlite field were obtained (exact pipes unknown) and are highly weathered and/or carbonated garnet websterites. They consist predominantly of coarse dark green clinopyroxene (≤6 mm) and deep red garnet (≤5 mm) (Fig. 2d) accompanied by various REE-rich accessory minerals such as monazite and apatite. Garnets from the Braúna field are Cr-pyrope with MgO 18.9–20.2 wt% and CaO 4.2–4.7 wt% and contain little Cr_2O_3 0.7–1.5 wt%, they classify as low-Cr G4 garnets according to the scheme of Grütter et al. (2004) (Fig. 3). Garnets from B-9 L has anomalously low MgO (12.2 wt%) and high CaO (11.2 wt%) compared to others in the suite. Only one Braúna xenolith (B-6I) contained olivine, which has Mg# 92.0. This sample also has aluminium-rich spinel with Cr# 2.9–4.0. Based upon the garnet chemistry, the Braúna xenoliths are likely classified as pyroxenites or websterites (Fig. 3).

Mineral trace elements

In situ trace element analyses were only conducted on individual garnet and clinopyroxene grains from the Redondão and Braúna suites, as garnet is absent in the Limeira suite and the samples were too small to disaggregate for clinopyroxene separates (Fig. 4a, b). CI chondrite-normalised REE patterns for garnet from both the Braúna and Redondão suites display negatively sloped patterns with low $LREE_N$ and high $HREE_N$, with average Braúna La/Yb_N = 0.013 and average Redondão La/Yb_N = 0.015 (Fig. 4c, d). Redondão garnet grains have an overall slightly greater concentration of REE compared to those from the Braúna websterites. Following the compositional populations of mantle-derived Cr-pyrope garnets defined by trace elements (Griffin et al. 1999, 2002), the Redondão suite falls approximately into the 'depleted/metasomatised peridotites' and 'melt-metasomatised peridotite' categories based upon mean concentrations of Y, Zr and Ti (Table 3) (Griffin et al. 2003). Clinopyroxene in Braúna and Redondão suites have convex REE_N patterns with LREE approximately 10× chondritic values, and low HREE ~ 0.15× chondrite (Fig. 4c, d). $LREE_N$ is enriched relative to both $MREE_N$ and $HREE_N$. Braúna clinopyroxenes are overall more enriched in REEs than Redondão, with La/Yb_N= 38.8 and 25.1, respectively. The Cpx_N/Grt_N REE show very similar trends across different samples (Fig. 4e), although B-5H, RE-02 and RE-04 show some dispersion.

PGE and $^{187}Os/^{188}Os$ ratios

Bulk rock platinum group element (PGE) and $^{187}Os/^{188}Os$ data were collected on the Redondão and Limeira peridotite xenoliths (Table 4). Although PGE data were collected from the Braúna pyroxenites, the concentrations were extremely low and the samples too over-spiked to give accurate results.

The two peridotite suites have broadly similar platinum group elements patterns, with elevated Os, Ir and Ru (I-PGE group) having typically higher PUM-normalised values than Pt and Pd (P-PGE group) (Fig. 5). When compared to the compilations of cratonic xenoliths and off-craton xenoliths (Aulbach et al. 2016), normalised I-PGE concentrations are like those of cratonic mantle, with relatively unfractionated Os/Ir ratios (Fig. 5). Distinctive exceptions are LIM-6, which has Os greater than primitive upper mantle, and RE-04, which has Ru greater than primitive upper mantle. Pt and Pd concentrations are closer to values from cratonic

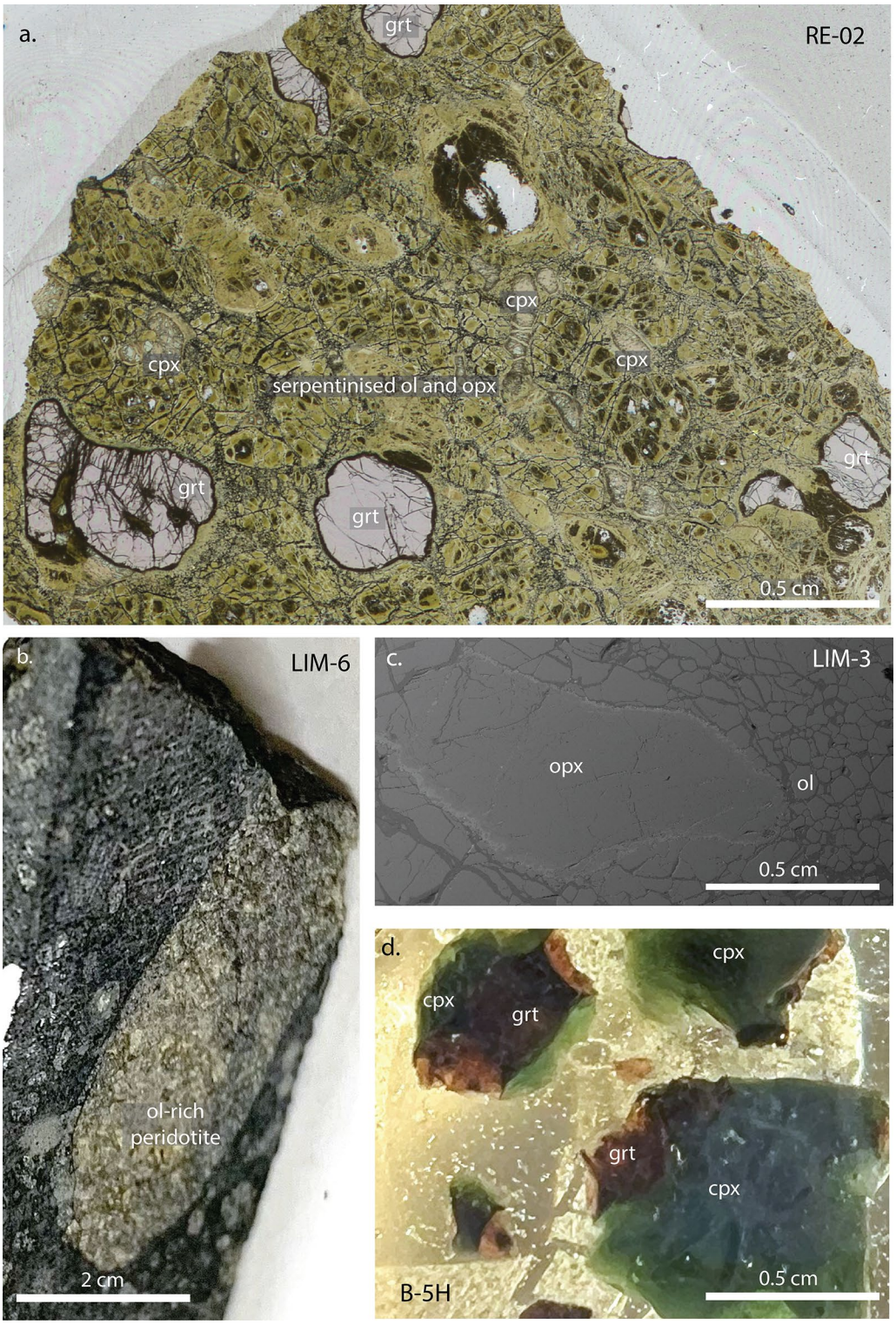

Fig. 2 Xenolith minerals and textures. **a** Redondão peridotite xenolith minerals, with the exception of garnet (grt), are extensively altered. Some relict clinopyroxene (cpx) and orthopyroxene (opx) (not visible in this field of view) are present. Sample RE-02. **b** The studied Limeira peridotites are small, mainly harzburgitic to dunitic fragments. **c** In some cases (e.g., LIM-3), there are porphyroclasts of orthopyroxene surrounded by variably recrystallised olivine (Ol), as seen in this back-scattered electron image. **d** The Braúna pyroxenites contain a deep red garnet and dark green clinopyroxene. Here, fragments of B-5 H are mounted in epoxy

Table 2 Mineral major element chemistry for mantle xenoliths from Limeira-1 (LIM), Brauna (B) and Redondão (RE) kimberlites

Ol	SiO_2	TiO_2	Al_2O_3	FeO	MnO	MgO	CaO	Na_2O	K_2O	Cr_2O_3	Total
LIM-1	41.26			7.33	0.27	51.44					100.30
LIM-2	40.54			8.92		49.66	0.16				99.28
LIM-3	41.21			7.50		51.33					100.03
LIM-4	42.00			7.57		49.59					99.15
LIM-5	41.51			7.46	0.40	51.47					100.84
LIM-6	41.38			7.33		51.62					100.34
LIM-7	41.19			7.44		51.89					100.53
B-6I	41.97			7.43		51.03					100.43
Opx	SiO_2	TiO_2	Al_2O_3	FeO	MnO	MgO	CaO	Na_2O	K_2O	Cr_2O_3	Total
LIM-2	56.65	0.23	1.20	5.19	0.12	34.97	0.79	0.04		0.54	99.73
LIM-5	57.85	0.22	1.30	4.47	0.08	34.80	0.66	0.06		0.31	100.46
B-6I	52.65	0.30	7.91	7.78	0.11	29.94	1.18	0.12		0.55	100.54
RE-01	57.07	0.27	1.53	4.96	0.04	34.89	1.01	0.11		0.52	100.39
RE-04	56.76	0.27	1.35	5.25	0.06	34.60	0.93	0.13		0.60	99.95
Cpx	SiO_2	TiO_2	Al_2O_3	FeO	MnO	MgO	CaO	Na_2O	K_2O	Cr_2O_3	Total
LIM-2	53.74	0.54	2.16	4.22	0.06	19.47	19.13	0.16		1.10	100.58
LIM-5	54.19	0.21	1.79	2.22	0.05	18.69	21.43	0.85		1.11	100.54
LIM-7	55.23	0.12	2.35	1.74	0.07	17.66	21.45	1.06		1.31	100.99
B-4G	56.13	0.15	2.46	2.95	0.09	16.51	19.71	1.68		0.74	100.41
B-5 H	55.69	0.18	4.34	5.67	0.13	17.03	14.73	1.92		0.33	100.01
B-6I	55.80	0.37	2.75	2.61	0.08	16.03	20.43	1.86		0.40	100.32
B-9 L	54.85	0.13	5.99	3.20	0.05	12.93	19.53	2.26		0.05	99.00
B-11 N	55.36	0.14	2.01	2.65	0.11	17.57	20.02	1.22		0.38	99.45
B-13P	55.18	0.84	0.84	1.98	0.10	16.33	24.79			0.41	100.46
RE-01	55.08	0.43	2.39	2.87	0.09	18.94	18.66	1.36		1.14	100.95
RE-02	54.10	0.30	2.20	2.87	0.06	18.56	18.93	1.27		1.32	99.61
RE-04	48.58	1.02	9.03	3.73	0.28	15.76	19.21	0.66		2.37	100.64
Grt	SiO_2	TiO_2	Al_2O_3	FeO	MnO	MgO	CaO	Na_2O	K_2O	Cr_2O_3	Total
B-4G	42.51	0.30	22.64	8.72	0.30	20.22	4.48			1.46	100.63
B-5 H	42.20	0.39	22.54	10.58	0.26	18.86	4.70			0.75	100.28
B-6I	42.25	0.40	23.53	8.02	0.34	20.63	4.18			0.65	99.98
B-9 L	40.01	0.22	24.19	12.13	0.27	12.19	11.12			0.24	100.37
B-11 N	42.43	0.30	23.08	6.85	0.32	21.55	4.29			1.05	99.86
RE-01	41.49	0.45	20.26	7.02	0.29	19.63	5.89			4.90	99.91
RE-02	41.32	0.80	19.89	7.23	0.29	18.72	5.57			6.99	100.81
Spl	SiO_2	TiO_2	Al_2O_3	FeO	MnO	MgO	CaO	Na_2O	K_2O	Cr_2O_3	Total
RE-04	41.95	0.44	20.81	6.67	0.26	20.46	5.33			4.28	100.19
LIM-1		0.12	15.06	18.66		12.66				53.70	100.20
LIM-7		0.14	27.85	18.14		12.38				42.22	100.72
RE-01		0.72	43.15	12.18		19.91				24.45	100.40
RE-02		0.31	52.53	11.59		20.19				14.97	99.59
RE-04		0.51	46.72	11.95	0.42	19.06				21.12	99.78

Concentrations of major oxides quoted in wt%The SEM limit of detection is <0.1 wt%

mantle than off-craton samples (0.36 and 0.14 ppb, respectively) (Aulbach et al. 2016). Rhenium is commonly added to peridotite xenoliths during entrainment and transport to the surface (Walker et al. 1989) and so the distribution of this element may not be related to the mantle source.

The Redondão peridotites have measured $^{187}Os/^{188}Os$ ranging between 0.11206 and 0.11939 and $^{187}Re/^{188}Os$ from 0.023 to 0.139 (Fig. 6a; Table 4). While there may be a subtle trend when plotted against anhydrous-normalised bulk Al_2O_3 or CaO, the few samples available make this a very weak correlation (Fig. 6b and c) (Table 5). Although the host Redondão kimberlite is undated, the age is assumed to be Cretaceous (Svisero et al. 1977; Almeida-Filho and Castelo Branco 1992), and initial Os isotopic ratios are calculated at 100 Ma, the assumed time of kimberlite eruption. This gives $^{187}Os/^{188}Os_i$ of 0.11202–0.11916, and assuming a Primitive Upper Mantle reservoir with a present-day $^{187}Os/^{188}Os$ of 0.1296 (Meisel et al. 2001), results in T_{RD} of 1.3–2.3 Ga

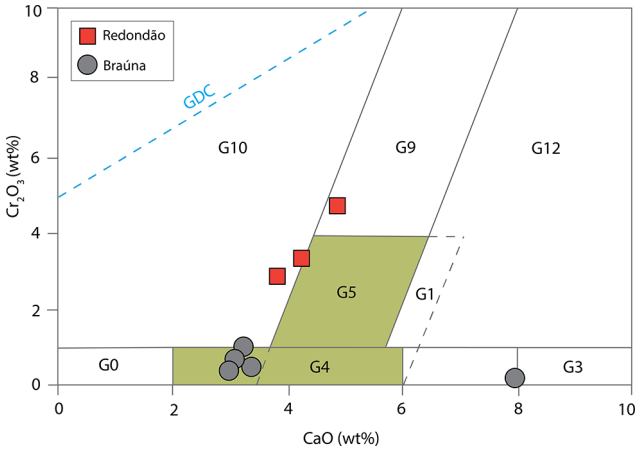

Fig. 3 Garnet Cr_2O_3-CaO classification plot after Grütter et al. (2004). Pyroxenitic categories (G5 and G4) are indicated by the green shaded pattern. Limeira-1 samples are not plotted here due to the absence of garnet. GDC refers to the graphite-diamond constraint for garnets under the G10 classification (Grütter et al. 2004)

(Fig. 7). Limeira peridotites have measured $^{187}Os/^{188}Os$ ranging between 0.1097 and 0.1170 and $^{187}Re/^{188}Os$ from 0.05 to 0.792 (Table 4). Age correction of these to the eruption age of 91 Ma (Guarino et al. 2013) gives $^{187}Os/^{188}Os_i$ of 0.10964–0.11576 (Table 4) and T_{RD} ages of 1.8 to 2.6 Ga (Fig. 7). These data are comparable to $^{187}Os/^{188}Os$ data from Tres Ranchos and other kimberlite-erupted xenoliths from the APIP and Coromandel kimberlite fields reported by Carlson et al. (2007), which have $^{187}Os/^{188}Os$ from 0.10990 to 0.11517 and eruption age corrected $^{187}Os/^{188}Os_i$ of 0.10572–0.11395. The Braúna pyroxenites have more radiogenic $^{187}Os/^{188}Os$ compared to the peridotite suites. Measured $^{187}Os/^{188}Os$ is between 0.12722 and 0.19210 and $^{187}Re/^{188}Os$ is 0.70321–1.34234, which corrects to $^{187}Os/^{188}Os_i$ 0.11896–0.36866 at 640 Ma.

Geothermobarometry

The Ni-in-garnet thermometer yields T_{Ni} from single garnet grains in harzburgite and lherzolite xenoliths via the exchange of Ni and Mg in garnet and olivine, assuming chemical equilibrium (Ryan et al. 1996; Canil 1999; Sudholz et al. 2021b). Temperatures obtained using the Ryan et al. (1996) method for Redondão garnets (RE-01, RE-02 and RE-04) gave T_{Ni} between 1253 and 1313 °C (Fig. 8; Table 6). The T_{Ni} thermometer was unsuitable for the majority of Braúna samples since there is no evidence of co-existing olivine, except for B-6I which yields a result of T_{Ni} = 1015 °C. The Brey and Köhler (1990) two-pyroxene thermometer was only able to be used to determine temperature estimates for LIM-2 and LIM-5, which returned 1072 and 1276 °C.

Due to small samples and coarse grain size, several different geothermobarometric methods are required. Fe-Mg exchange reactions between garnet and clinopyroxene allow equilibrium temperatures of mantle xenoliths to be calculated. Using the Sudholz et al. (2022) Fe-Mg exchange thermometry between garnet and clinopyroxene, calculated with preset temperatures and coupled with the Cr-in-clinopyroxene single crystal geobarometer of (Sudholz et al. 2021a) recalibrated from Nimis and Taylor (2000), a temperature interval of 1007–1277 °C and 1.9–2.8 GPa (av = 2.4 GPa) is determined for the Braúna suite (Table 6). The Cr-in-clinopyroxene thermobarometer was only applicable to B-4G and B-11 N due to insufficient clinopyroxene Cr# in the other samples. The Redondão peridotites returned temperatures between 1119 and 1393 °C and pressures between 3.5 and 4.9 GPa using this thermobarometer combination (Table 6; Fig. 8).

Discussion

Age, composition and depths of extraction of the regional mantle lithosphere

Previous studies have determined that the lithosphere beneath portions of the São Francisco Craton have geothermal gradients of ~35 to 42 mW/m^2 (Pereira et al., unpublished data; Carvalho et al. 2022) and is therefore cold and thick. The olivine Mg#, bulk rock compositions, the $^{187}Os/^{188}Os$ data, and minimum T_{RD} (1.8 to 3.2 Ga) of the Limeira peridotites (this study; Carlson et al. 2007), which are derived from outside the classically-drawn boundaries of the craton nucleus, confirm the existence of refractory Paleoproterozoic to Neoarchean mantle lithosphere beneath this area. Their garnet-free nature may be due to the greatly expanded stability of spinel in Cr-rich peridotites (spinel Cr# 70–89) (Klemme 2004), or alternatively, the depleted mantle may not have had sufficient Al available to form garnet. In any case, it is evident that the mantle lithosphere sampled by this kimberlite was also cold and old.

The P-T data for the Redondão garnet peridotites indicate that the lithosphere there is at least up to ~160 km, with the new Paleoproterozoic–Mesoproterozoic minimum T_{RD} ages (1.3–2.2 Ga) contrasting greatly with the Palaeozoic to Mesozoic exposed crust (Svisero et al. 1977, 1984). In instances where there is no fresh olivine, such as for the Redondão xenoliths, the degree of peridotite depletion may be estimated by the Cr_2O_3 in garnet. Pyrope garnets from global Archean suites (>2.5 Ga) have 3.5–7.3 wt% Cr_2O_3, Paleo- and Mesoproterozoic age suites have 2.6–6.0 wt% Cr_2O_3 and Neoproterozoic suites tend to have much lower Cr_2O_3 of 1.7–2.8 wt% (Griffin et al. 1999). Although the Cr

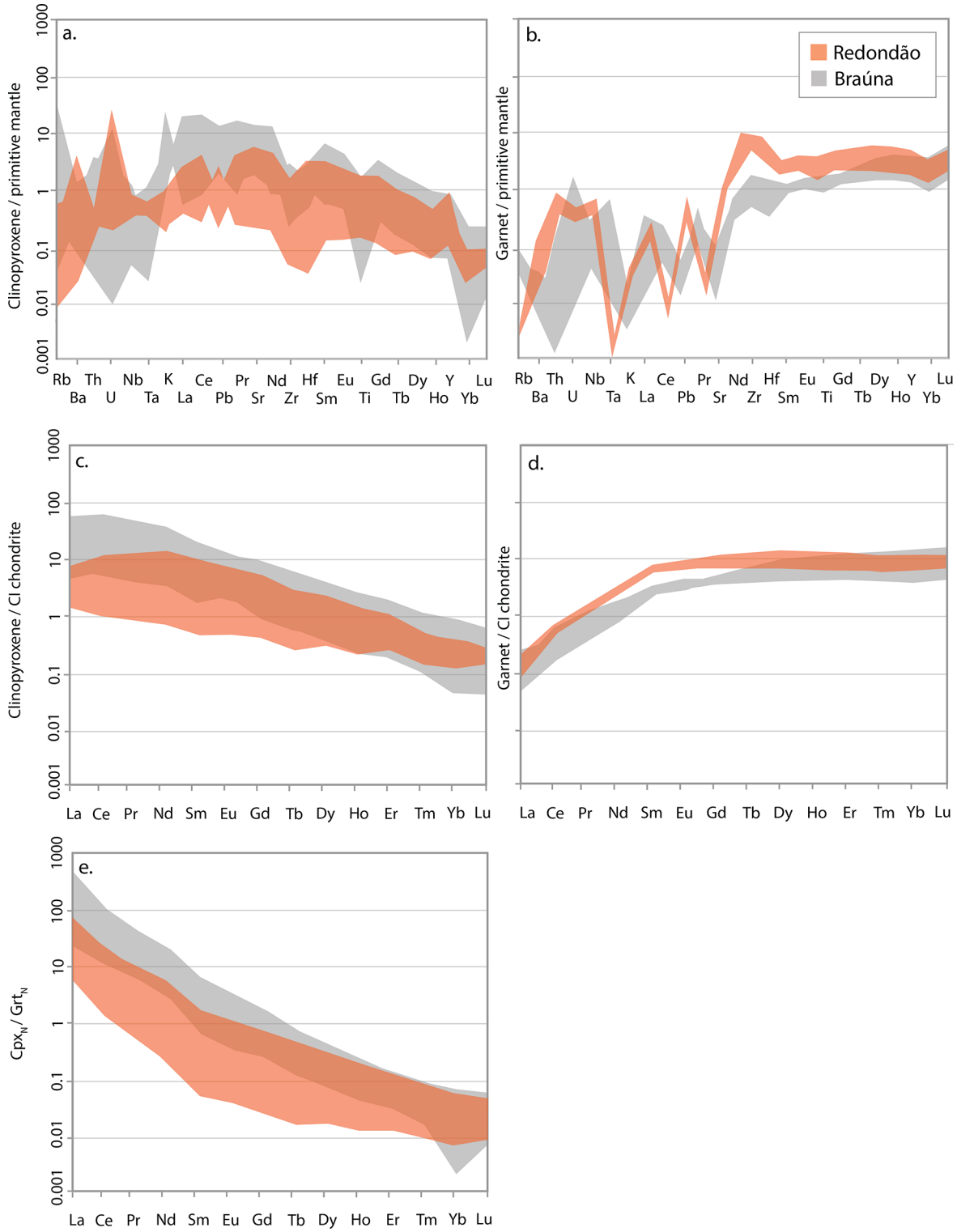

Fig. 4 **a**, **b** In situ trace elements for clinopyroxene and garnet normalised to PUM (Sun and McDonough, 1995). **c**, **d** In situ rare earth elements for clinopyroxene and garnet normalised to CI chondrite (Sun and McDonough, 1995) **e** $Cpx_N/Grt/_N$ REE plot. Limeira-1 samples are not plotted here due to the absence of garnet and insufficient clinopyroxene

Table 3 In situ clinopyroxene (Cpx) and garnet (Grt) trace element concentrations for Brauna (B-) and Redondão xenoliths (RE-)

Mineral	Cpx									Grt							
Sample	B-4G	B-5H	B-6I	B-9L	B-10M	B-11N	RE-01	RE-02	RE-04	B-4G	B-5H	B-6I	B-9L	B-11N	RE-01	RE-02	RE-04
Rb	0.20	0.12	0.08	0.20	11.3	0.09	0.02	0.18	0.40	0.17	0.00	0.00	0.12	0.20	0.00	0.00	0.00
Ba	8.6	1.3	3.6	0.63	7.2	1.2	0.22	24.1	5.5	0.09	0.00	0.11	0.61	0.48	0.00	0.10	0.00
Th	0.13	0.00	0.30	0.00	0.15	0.03	0.03	0.28	0.04	0.01	0.00	0.01	0.01	0.00	0.00	0.01	0.01
U	0.01	0.00	0.05	0.00	0.28	0.00	0.01	0.42	0.03	0.01	0.00	0.03	0.00	0.00	0.01	0.02	0.01
Nb	0.52	0.04	0.82	0.04	0.18	0.39	0.26	0.67	0.35	0.17	0.03	0.14	0.03	0.20	0.24	0.32	0.23
Ta	0.03	0.00	0.01	0.00	0.01	0.04	0.03	0.04	0.02	0.01	0.00	0.00	0.00	0.02	0.01	0.03	0.02
K	1005	2428	366	4990	584	1065	248	65.7	59.6	3.1	0.00	8.2	15.6	11.8	0.00	3.0	0.00
La	3.0	1.1	12.9	0.43	2.9	4.5	1.8	0.32	1.3	0.01	0.02	0.03	0.02	0.22	0.02	0.03	0.03
Ce	9.2	3.8	35.8	1.7	4.5	12.8	6.9	0.55	3.7	0.11	0.22	0.38	0.15	0.39	0.31	0.38	0.35
Pb	0.76	0.42	2.3	0.44	1.2	0.59	0.15	0.47	0.07	0.02	0.00	0.04	0.01	0.03	0.00	0.01	0.01
Pr	1.4	0.63	4.3	0.27	0.40	1.9	1.2	0.08	0.46	0.04	0.07	0.11	0.04	0.07	0.12	0.14	0.13
Sr	128	293	285	149	40.9	192	120	4.8	6.3	0.41	1.88	0.53	1.0	0.26	0.37	0.44	0.42
Nd	6.8	3.3	16.9	1.3	1.5	7.8	6.1	0.31	1.9	0.40	0.75	0.89	0.43	0.63	1.3	1.5	1.5
Zr	3.3	5.3	17.8	10.44	25.5	2.7	17.2	0.72	1.6	7.0	18.5	18.4	5.9	11.4	59.4	97.46	57.4
Hf	0.17	0.26	0.84	0.38	0.36	0.23	1.0	0.02	0.08	0.14	0.43	0.35	0.11	0.33	1.3	2.3	1.2
Sm	1.5	0.75	2.8	0.29	0.25	1.3	1.4	0.07	0.49	0.39	0.52	0.43	0.39	0.39	0.92	1.3	1.1
Eu	0.39	0.25	0.71	0.09	0.11	0.35	0.41	0.03	0.17	0.18	0.25	0.21	0.24	0.18	0.40	0.60	0.50
Ti	854	1098	1944	934	49.3	930	2340	240	1645	1224	2090	2070	1222	1454	2300	4410	2540
Gd	0.93	0.62	1.9	0.21	0.19	1.1	1.1	0.09	0.58	0.77	0.88	1.0	0.78	0.96	1.5	2.6	1.9
Tb	0.09	0.08	0.21	0.02	0.02	0.14	0.12	0.01	0.07	0.17	0.18	0.26	0.15	0.24	0.26	0.51	0.35
Dy	0.43	0.42	1.0	0.09	0.11	0.73	0.56	0.08	0.35	1.3	1.5	2.4	1.1	2.3	1.8	3.8	2.6
Ho	0.06	0.07	0.15	0.01	0.02	0.12	0.08	0.01	0.07	0.30	0.36	0.62	0.25	0.58	0.37	0.82	0.56
Y	1.4	1.7	3.6	0.32	0.66	2.6	1.7	0.63	4.0	7.8	9.6	16.3	6.4	15.1	9.5	20.1	14.6
Yb	0.05	0.10	0.15	0.00	0.04	0.13	0.07	0.03	0.03	0.93	1.3	2.4	0.70	2.3	1.1	2.1	1.8
Lu	0.00	0.01	0.02	0.00	0.01	0.01	0.01	0.00	0.00	0.14	0.22	0.39	0.11	0.34	0.17	0.31	0.27
Ni	562	341	362	471	24.2	514	499	2960	2090	78.0	89.4	46.5	59.4	76.5	89.4	405	100

All concentrations are un-normalised and are quoted in ppm

concentration is a function of the degree of depletion, and it is being increasingly recognised that there are ultra-refractory mantle lithospheres formed in the post-Archean Earth (Scott et al. 2020; Barrett et al. 2022), the occurrence of high Cr-pyrope garnets in mantle xenoliths from the Redondão kimberlite (4.3–7.0 wt% Cr_2O_3) (Table 4) suggests a refractory sub-continental lithospheric mantle. Thus, the chemical and isotopic data indicate that the mantle lithosphere represented by the Redondão xenoliths is old and cold, despite also being outside the classically drawn craton limits.

Extension of the craton to include kimberlite regions (APIP, Redondão)

Properties of the Limeira and Redondão peridotites coupled with recent geophysical models offer a revised interpretation of the extent of the São Francisco Craton. Key to this argument is that despite the crust being "off-craton", the mantle lithosphere beneath these locations meets the Pearson et al. (2021) definition of being cratonic; that is, the lithosphere-asthenosphere boundary (LAB) extends to >150 km depth and has been stable for ca. 1 Ga. The application of the Schaeffer and Lebedev (2013) tomographic model to South America illustrates changes in S-wave velocity in 2-dimensional slices at depths of 150, 175 and 200 km (Fig. 9a, b, c). High velocity anomalies at depths exceeding 175 km (Fig. 9b) occur beneath the north-eastern extent of the São Francisco Craton in the Borborema Province, and beneath a large region to the south-western region of the craton, encompassing the APIP (Limeira) and Brasilia Belt orogeny. Velocities are slightly lower to the north of the craton, encompassing the Redondão kimberlite, which may be due to post-cratonic lithospheric thinning (Rocha et al. 2019a; Celli et al. 2020).

Tomographical studies have also identified the high velocity signature in the lithospheric mantle to the south-west of the craton (Assumpçao et al. 2004; Rocha et al. 2011, 2019a; Assumpção et al. 2017; Celli et al. 2020), with some suggesting that the São Francisco Craton could be part of a much larger continental block (Pereira and Fuck 2005). Most of the models associated with the São Francisco Craton predict a maximum cratonic root depth between 200 and 250 km. Our thermobarometrical data suggest xenolith extraction depths are between ~120–160 km and at temperatures lower than what the LAB is typically considered (ca. 1350 °C), which means that the lithosphere must extend deeper than 160 km. Lower velocity regions correspond to known basins, such as the Paraná and Parnaíba basins and the Transbrasiliano Lineament (Fig. 9), which would have been subject to significant lithospheric reworking and deformation during their Neoproterozoic formation (Rocha et al. 2019b). Between 150 and 175 km depth, the São Francisco Craton appears to diverge into two lobes separated by a region of low velocity (Fig. 9a, b). An explanation for the subsurface topography of the craton may be due to lithospheric thinning by the Pirapora aulacogen, an aborted Proterozoic rift structure relict from the breakup of Gondwana (Alkmim et al. 2007; Rocha et al. 2019a; Teixeira et al. 2021), although higher resolution seismic data are needed to properly evaluate this. We examine the extent in more detail below.

The SW extent of the São Francisco Craton beneath the APIP

The presence of a cratonic root underneath the APIP, to the west of the São Francisco Craton surface-mapped extent, has been inferred in multiple studies (Carlson et al. 2007; Assumpção et al. 2017; Teixeira et al. 2017; Fernandes et al. 2021; Azzone et al. 2022; Carvalho et al. 2022; Guarino et al. 2024). Regions of anomalously high P and S-wave seismic velocity, low density, resistive electric response, low temperature and thus higher magnetic susceptibility, are well documented and correlated with global cratons and Precambrian shields (Polet and Anderson 1995; Artemieva 2011; Pearson et al. 2021; Ciardelli et al. 2022). High velocity anomalies (HVAs) suggest the presence of cold, chemically distinct mantle, one that is olivine rich and FeO-poor (Frederiksen et al. 2001).

The NE limit of the São Francisco Craton with the Borborema Province

The north-eastern margin between the São Francisco Craton and the Borborema province (Fig. 9) is tectonically and stratigraphically complex as a result of several episodes of collisional tectonics and magmatism since their amalgamation as part of west Gondwana between 590 and 570 Ma (Ganade de Araujo et al. 2014). The Borborema Province is believed to be a rifted fragment of the Benino-Nigerian Shield (de Souza Filho and Seoane 2022), segregated by extensive E-W trending shear zones that occurred during the late-Neoproterozoic Brasiliano orogeny (Hasui 2012; Neves 2021). Lithospheric discontinuities beneath the Pernambuco Lineament, an extensive shear zone, represented by a transition from conductive to resistive lithosphere and a northward gradient of high to low P-wave velocity anomalies (Rocha et al. 2019a), suggest a progression from stable cratonic lithosphere to one that is thin and/or modified (Santos et al. 2014; Rocha et al. 2019a; de Souza Filho and Seoane 2024). The S-wave tomographical model of Schaeffer and Lebedev (2013) supports the existence of thick cratonic lithosphere extending north of the conventionally defined São Francisco Craton into the southern Borborema

Table 4 Rhenium-Os isotopes and HSE abundances for Brazilian mantle xenoliths from Limeira-1 (LIM), Brauna (B) and Redondão (RE) kimberlites

Sample	Os ppb	Ir ppb	Ru ppb	Pt ppb	Pd ppb	Re ppb	$^{187}Re/^{188}Os$	error 2se	$^{187}Os/^{188}Os$	error 2se2	$^{187}Os/^{188}Osi$	T_{RD} Ga	$T_{RD\,(eruption)}$	Ol Mg#	Spl Cr#
LIM-1	2.00	0.78	3.59	0.43	0.14	0.06	0.15106	0.00458	0.11094	0.00017	0.11071	2.40	2.49	92.6	70.5
LIM-2	2.96	2.08	4.45	1.47	0.85	0.16	0.25948	0.00781	0.11166	0.00018	0.11127	2.30	2.42	91.3	
LIM-4	2.41	3.32	6.98	1.21	0.19	0.17	0.34368	0.01037	0.11213	0.00018	0.11161	2.23	2.37	92.5	
LIM-5	2.62	1.38	3.02	1.36	2.18	0.31	0.05617	0.00170	0.11095	0.00021	0.11087	2.40	2.47	92.2	89.5
LIM-6	7.25	4.01	8.96	0.48	0.22	0.07	0.04902	0.00144	0.10971	0.00016	0.10964	2.57	2.64	92.5	
LIM-7	1.93	1.31	3.13	0.34	0.08	0.32	0.79212	0.02639	0.11696	0.00028	0.11576	1.57	1.80	92.6	50.4
RE-01	3.26	3.24	5.89	3.67	1.73	0.09	0.13004	0.00364	0.11247	0.00016	0.11226	2.19	2.28	92.7	
RE-02	1.79	1.74		2.48	0.68	0.05	0.13878	0.01001	0.11939	0.00021	0.11916	1.23	1.33		
RE-04	2.47	3.74	32.51	2.15	0.64	0.01	0.02282	0.00581	0.11206	0.00016	0.11202	2.24	2.31		
B-4G	1.87	1.89	5.35	17.71	13.43	0.35	0.90710	0.04770	0.17889	0.00031	0.16917				
B-5 H	0.62	0.61	1.19	0.84	0.69	0.10	0.77105	0.03698	0.12722	0.00023	0.11896				
B-6I	0.28	0.24	0.88	2.82	2.48	0.40	0.70321	0.39855	0.37620	0.00079	0.36866			92.0	2.5
B-9 L	1.03	0.91	2.16	3.61	2.57	0.19	0.87207	0.03966	0.15647	0.00025	0.14713				4.0
B-10 M	0.01	0.01	0.03	0.27	0.11	0.09									
B-11 N	0.70	0.87	2.31	18.24	18.62	0.19	1.34324	0.05846	0.19210	0.00030	0.17770				1.0

Limeira-1 eruption age = 91 Ma

Redondão eruption age (estimated) = 100 Ma

2SE= 2 standard error

Province, potentially to the juncture of a paleo-suture zone formed between two continental blocks (Fig. 9). Alternatively, these high velocity anomalies observed to the north of the São Francisco Craton may be generated by the northward subducted São Francisco paleo-slab underneath the Borborema province (de Oliveira et al. 2023). We therefore suggest that the northern lithospheric boundary of the São Francisco Craton is approximately beneath the Pernambuco Lineament, despite the surface representation of the craton being somewhat southward, within the Rio Preto, Riacho do Pontal and Sergipana fold and thrust belts (Fig. 1) (Ganade et al. 2021; Neves 2021; de Souza Filho and Seoane 2024).

The W limit of the São Francisco Craton with the transbrasiliano lineament and Parnaiba block

The western São Francisco cratonic margin with the Borborema Province and the Amazonian Craton is overlain by the Parnaíba intracratonic basin, which is underpinned by high to moderately resistive regions in the upper mantle that are representative of relict continental lithosphere (de Souza Filho and Seoane 2024). Low P-wave velocity anomalies trending NE-SW are in agreement with the orientation of the Transbrasiliano Lineament (Fig. 9), a ~ 200 km wide feature separating the São Francisco and Amazonian paleo plates which were merged during a series of collisions between 950 and 550 Ma (de Azevedo et al. 2015). This region of anomalously low velocity between the Amazonian and São Francisco cratons is interpreted as the approximate location of the upper mantle boundary zone.

The SW limit of the São Francisco Craton with the Paranapanema block

S-wave tomographic slices of the lithosphere from Schaeffer and Lebedev (2013) (Fig. 9) display sustained high velocity anomalies until ~ 175 km depth (Fig. 9b) to the south-west of the São Francisco Craton extending beneath the APIP and Paranapanema cratonic block which is obscured at the surface by the Paraná sedimentary basin and flood basalts (Rocha et al. 2011, 2019b). The Paranapanema block has been described as both a cohesive cratonic block (Cordani et al. 1984; Mantovani and de Brito Neves 2005) and as an accumulation of multiple lithospheric fragments separated by suture zones (Rocha et al. 2011). Low velocity anomalies coincide closely with the suggested limits of the lithospheric feature (Milani and Ramos 1998; Rocha et al. 2011). Collisional magmatism in the region at 790 Ma has been interpreted to mark approximate closure between the Paranapanema and greater São Francsico Craton (Heilbron et al. 2017; Rocha et al. 2019b). Although the cratonic lithosphere of the São Francisco Craton and Paranapanema block

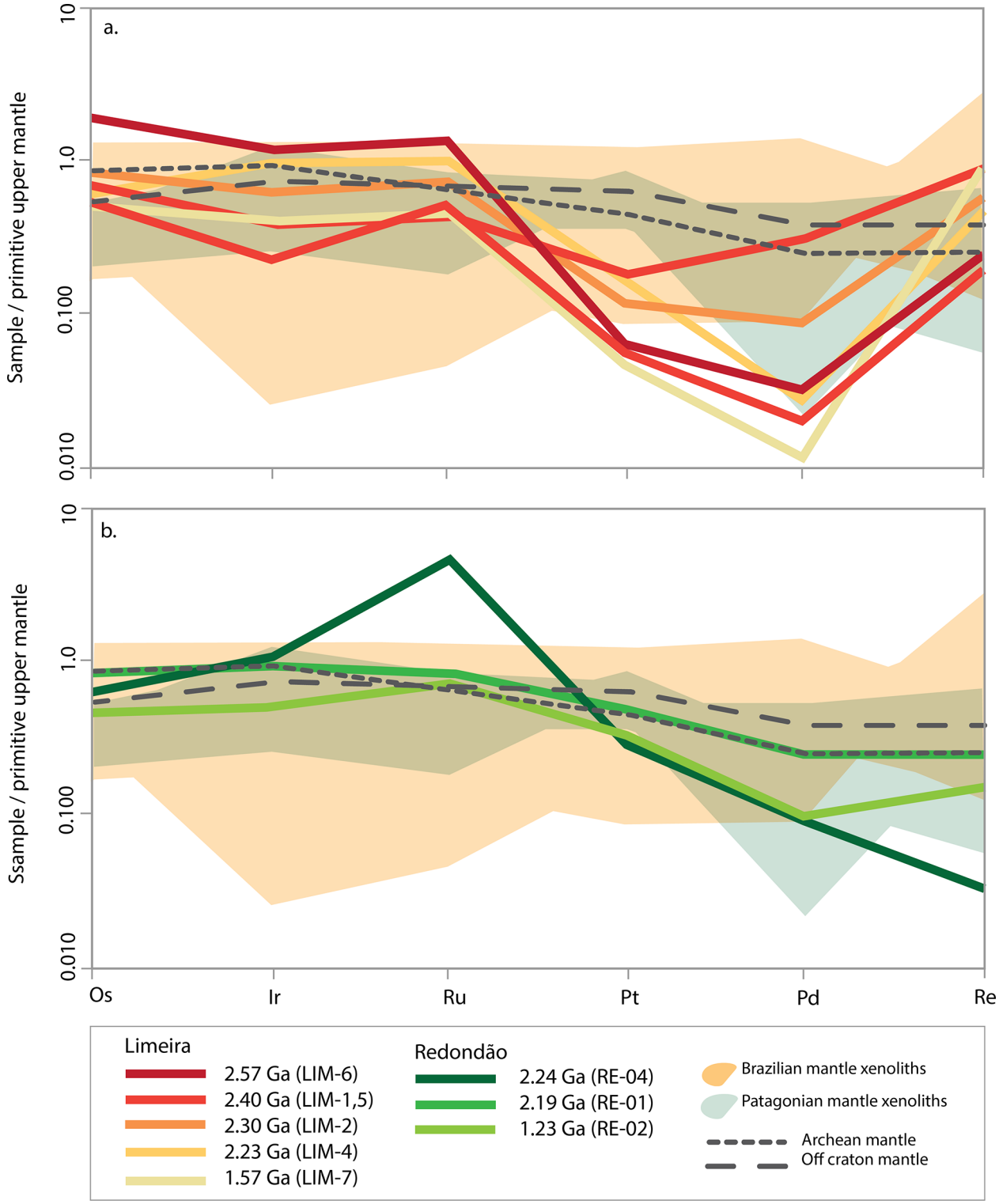

Fig. 5 **a** Platinum group elements in Limeira and **b** Redondão peridotites normalised against Primitive Upper Mantle from Becker et al. (2006). Brauna samples are omitted because of low concentrations due to over spiking. Archean and off-craton mantle values from Aulbach et al. (2016). Shaded regions represent samples from elsewhere across the South American continent. Brazilian mantle xenolith field from Carlson et al. (2007); Ngonge et al. (2019), Patagonian mantle xenolith field from Schilling et al. (2008); Mundl et al. (2016); Schilling et al. (2017)

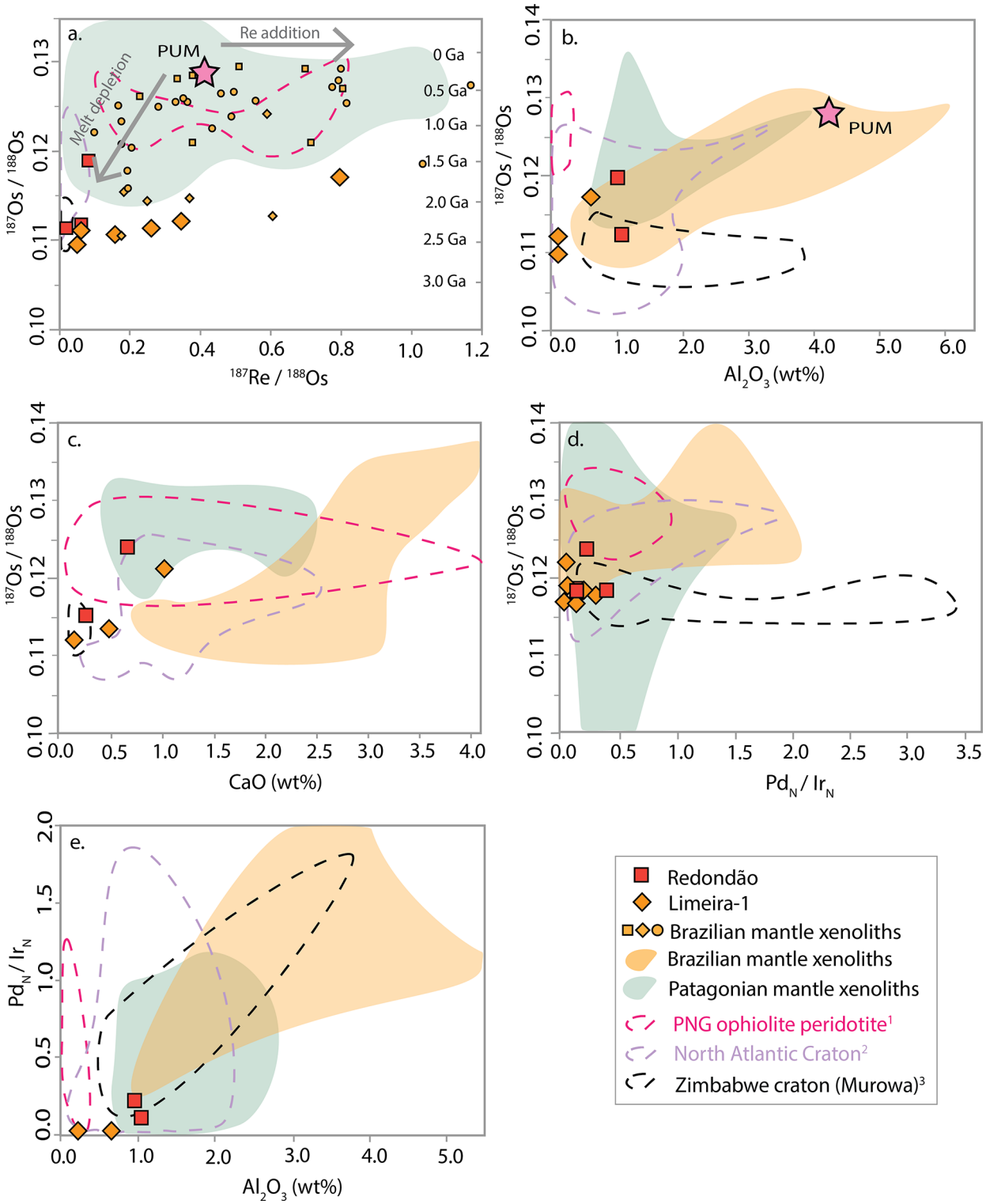

Fig. 6 **a** $^{187}Os/^{188}Os$ vs. $^{187}Re/^{188}Os$, PUM value from Meisel et al. 2001 ($^{187}Os/^{188}Os$ = 0.129, $^{187}Re/^{188}Os$ = 0.42). Brazilian mantle xenolith suites include Macau volcanic field (small circles), Tres Ranchos (small diamonds), Parauna (small squares). **b** $^{187}Os/^{188}Os$ plotted against Al_2O_3 as a melt depletion index (Aulbach et al. 2016) **c** $^{187}Os/^{188}Os$ plotted against CaO. **d** $^{187}Os/^{188}Os$ plotted against Pd_N/Ir_N. **e** Pd_N/Ir_N versus bulk Al_2O_3. Brazilian mantle xenolith suites are from Carlson et al. (2007); Ngonge et al. (2019), Patagonian mantle xenolith suites are from Schilling et al. (2008); Mundl et al. (2016); Schilling et al. (2017). PNG ophiolite peridotite from Barrett et al. (2020), North Atlantic Craton from Wittig et al. (2010) and Zimbabwe Craton values are from Smith et al. (2009)

Table 5 Bulk rock and trace element chemistry for mantle xenoliths from Limeira-1 (LIM), Brauna (B) and Redondão (RE) kimberlites

Sample	RE-01	RE-02	RE-04	B-4G	B-5 H	B-6I	B-9 L	B-10 M	B-11 *N*	LIM-01	LIM-6	LIM-7
Major oxides (wt%)												
SiO_2	47.05	47.95	46.59	47.28	49.60	44.78	44.81	38.04	45.74	40.70	40.70	42.98
TiO_2	0.08	0.09	0.08	0.24	0.99	0.38	0.45	0.32	0.41	0.00	0.00	0.01
Al_2O_3	0.77	0.99	1.04	12.38	6.44	17.06	14.97	16.42	13.52	0.10	0.10	0.58
Fe_2O_3T	8.48	8.95	9.23	6.00	7.29	6.55	6.67	4.90	7.76	8.07	8.22	7.55
MnO	0.08	0.10	0.07	0.20	0.14	0.24	0.22	0.10	0.15	0.10	0.11	0.11
MgO	43.06	41.01	42.41	23.25	20.74	21.79	22.90	21.39	15.44	50.18	50.59	47.19
CaO	0.26	0.65	0.24	8.34	11.64	7.39	7.63	17.35	15.01	0.48	0.13	1.03
Na_2O	0.07	0.07	0.05	0.62	1.30	0.54	0.36	0.15	0.77	0.09	0.08	0.11
K_2O	0.01	0.02	0.02	1.59	1.61	0.89	1.24	1.02	0.99	0.04	0.03	0.14
Cr_2O_3	0.13	0.17	0.24	0.01	0.02	0.30	0.67	0.23	0.12	0.01	0.02	0.30
P_2O_5	0.01	0.02	0.03	0.10	0.23	0.07	0.06	0.08	0.08	0.23	0.01	0.01
Total	100.00	100.00	100.00	100.00	100.00	100.00	100.00	100.00	100.00	100.00	100.00	100.00
Trace elements (ppm)												
Rb	1.2	1.4	1.2	45.6	63.5	23.6	42.3	37.3	27.2	<1	<1	4.9
Sr	11.0	27.0	6.0	614	381	204	193	428	230	15.0	13.0	96.0
Y	3.5	4.5	0.90									
Zr	10.0	13.0	13.0	25.0	84.0	34.0	38.0	143.0	37.0	7.0	6.0	4.0
V	31.0	27.0	33.0	173.0	193.0	210.0	253.0	24.0	174.0	10.0	8.0	30.0
Ni	2266	2666	2494									
Cr	1338	1659	2426	112	226	3007	6675	2318	1230	112	226	3007
Nb	<0.5	<0.5	<0.5									
Ga	<1	<1	<1									
Cu	2.00	<2	<2									
Zn	47.0	47.0	50.0									
Co	110	135	121									
Ba	152	329	54	4559	1295	7520	2088	1180	5056	31.0	38.0	82.0
La	<2	<2	<2									
Ce	<2	<2	<2									
U	0.80	<0.5	0.50									
Th	<0.5	<0.5	<0.5									
Sc	2.0	2.0	4.0									
Pb	1.0	1.0	1.0									

Bulk rock compositions are normalised to anhydrous wt%

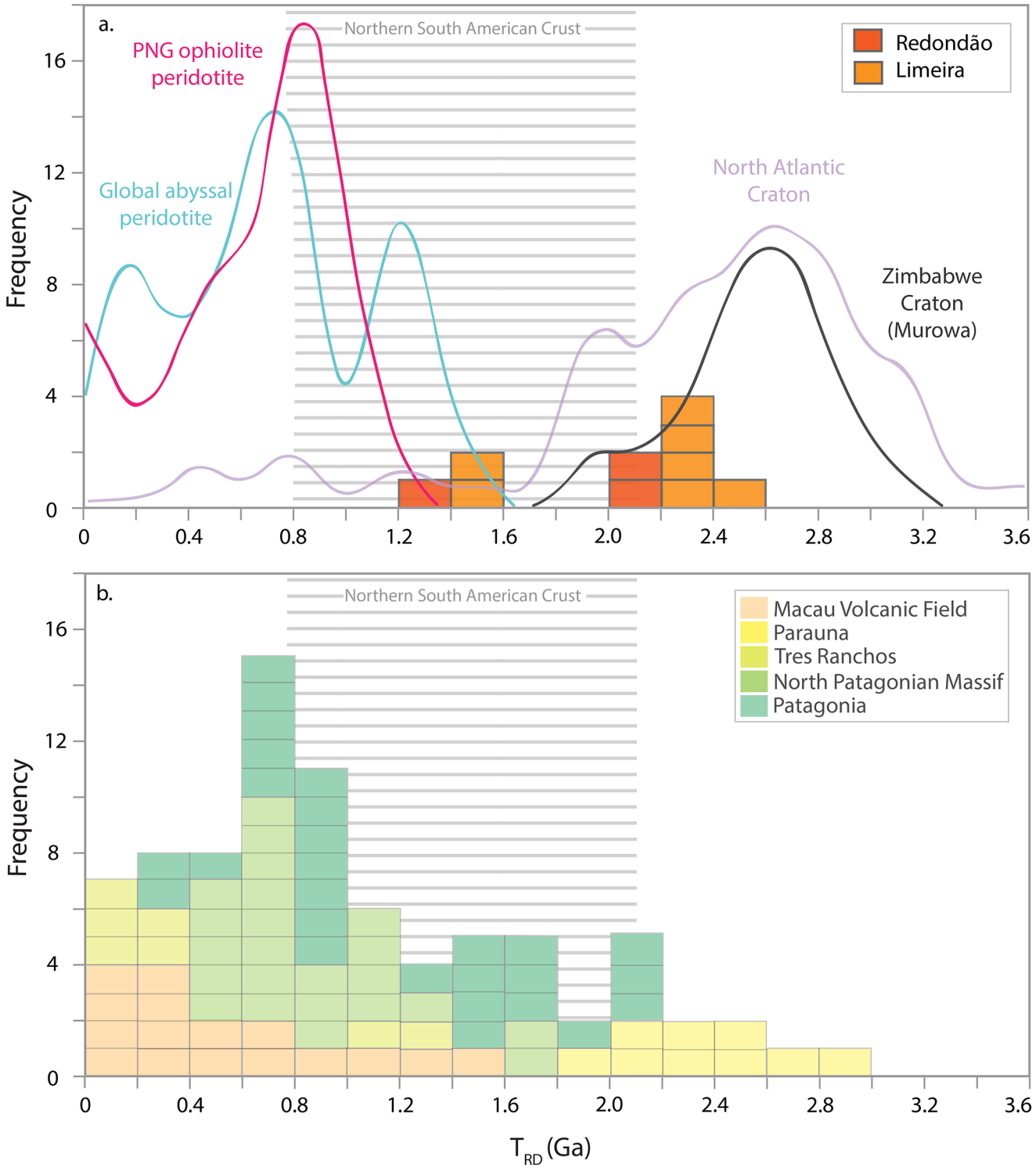

Fig. 7 Summary histogram showing the distribution of Re-depletion Os model ages T_{RD} (Ga) for South American mantle xenoliths compared to Archean, ophiolitic and abyssal xenolith suites. Global abyssal peridotite and Papua New Guinea (PNG) ophiolite peridotite represent Os isotopic compositions of the modern convecting mantle, values are from Barrett et al. (2022). North Atlantic Craton values are from Wittig et al. (2010) and the Zimbabwe Craton values are from Smith et al. (2009). Brazilian mantle xenolith suites are from Carlson et al. (2007); Ngonge et al. (2019), Patagonian mantle xenolith suites are from Schilling et al. (2008); Mundl et al. (2016); Schilling et al. (2017). Global curves only show relative distribution of probability and do not correspond to the same y-axis scale as the histogram data

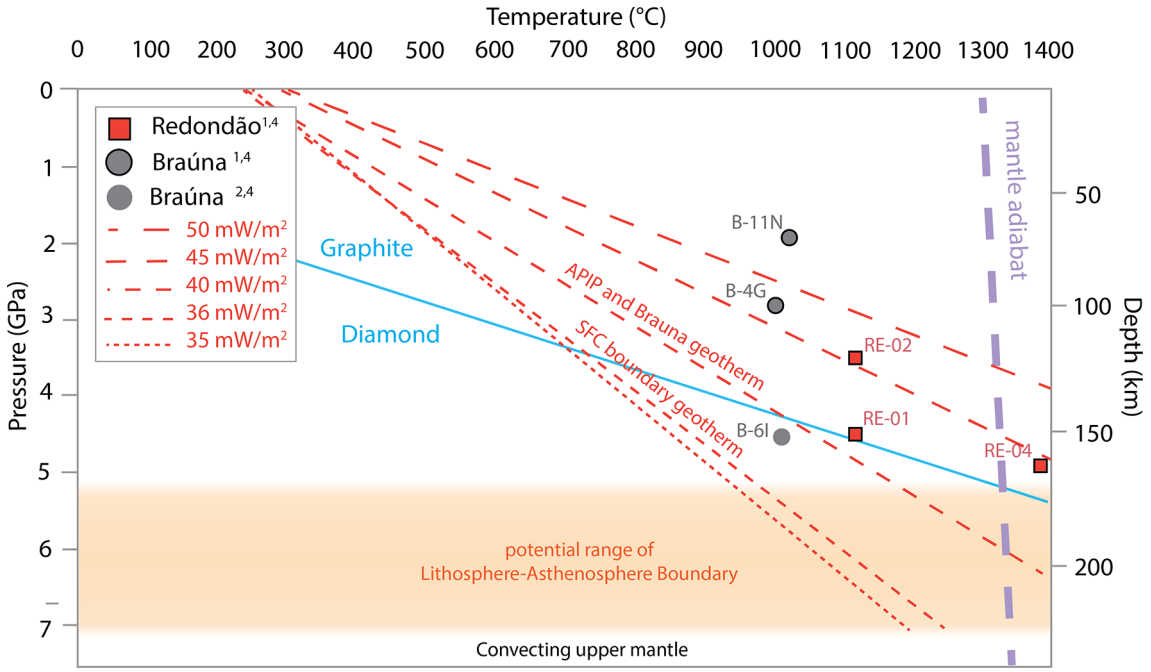

Fig. 8 Pressure temperature estimates for mantle xenoliths from Redondão, Braúna and Limeira kimberlites. 40 mW/m^2 geotherms for the Braúna and APIP mantle lithosphere (Pisani 2001; Carvalho et al. 2022) are slightly warmer than geotherms predicted for the São Franciso cratonic boundary (36 mW/m^2) and estimate the intercept between the mantle adiabat (Hasterok and Chapman 2011) and LAB at 160–220 km depth. [1]T[SUD22grt-cpx] (Sudholz et al. 2022),[2] TNi (Ryan et al. 1996),[3] T [BKN] (Brey and Köhler 1990),[4] P[SUDcpx] (Sudholz et al. 2022)

Table 6 Summary of temperature and pressure estimates for mantle xenoliths from Limeira-1 (LIM), Brauna (B) and Redondão (RE) kimberlites

Sample	Temperature	Pressure
LIM-2	1276 [3]	
LIM-5	1072 [3]	
B-4G	1007 [1]	2.8 [4]
B-5 H	1277 [1]	
B-6I	1015 [2]	
B-9 L	1078 [1]	
B-11 N	1025 [1]	1.9 [4]
RE-01	1260 [2], 1122 [1]	4.5 [4]
RE-02	1253 [2], 1119 [1]	3.4 [4]
RE-04	1313 [2], 1393 [1]	4.9 [4]

[1] T [Sud22$_{gnt\text{-}cpx}$] from Sudholz et al. (2022),[2] T$_{Ni}$ from Ryan and Griffin (1996), [3] T [BKN] from Brey and Kohler (1990), [4] P [Sud-22$_{cpx}$] from Sudholz et al. (2021)

were accreted together < 1 Ga, tomographic velocity models imply a continuation of thick lithosphere between the two, potentially representing a sutured interface. Nonetheless, the resolution of the model is approximately 200 km, and therefore it may not be high enough to distinguish two formerly separate blocks. For this reason, we include up to the interface zone between the São Francisco Craton and Paranapanema block in our revised craton limits (Fig. 9d). Although the age of collision being less than ~1 Ga (ca. 790 Ma) would exclude the Paranapanema block from being part of the São Francsico Craton in the Pearson et al. (2021) classification, their 1 Ga age is only a guideline, and these two blocks have been joined and stabilised for a period far longer than typical for orogens. Thus, the two blocks are on track to being cratonised and incorporated on this basis.

The E limit of the São Francisco Craton including the Araçuaí belt

High velocities also observed beneath the Araçuaí orogenic belt imply that cratonic mantle extends eastward of the surface expression of the São Francisco Craton (Fig. 9), underpinning a complicated and modified amalgamation of reworked São Francisco Craton Archean and Paleoproterozoic crustal terranes (Noce et al. 2007; de Morisson Valeriano et al. 2016; Rocha et al. 2019a). Various suggestions of the connection between the São Fransico Craton and the Congo Craton following the Araçuaí belt N-S during the formation of the Atlantic Ocean have been made (Rocha et al. 2019a and references therein). Given the evidence for the Araçuaí belt being a highly modified region of São Francisco cratonic basement and observations of subsurface cratonic features, we suggest that the São Francisco Craton margins extend to include the surrounding orogenic belts.

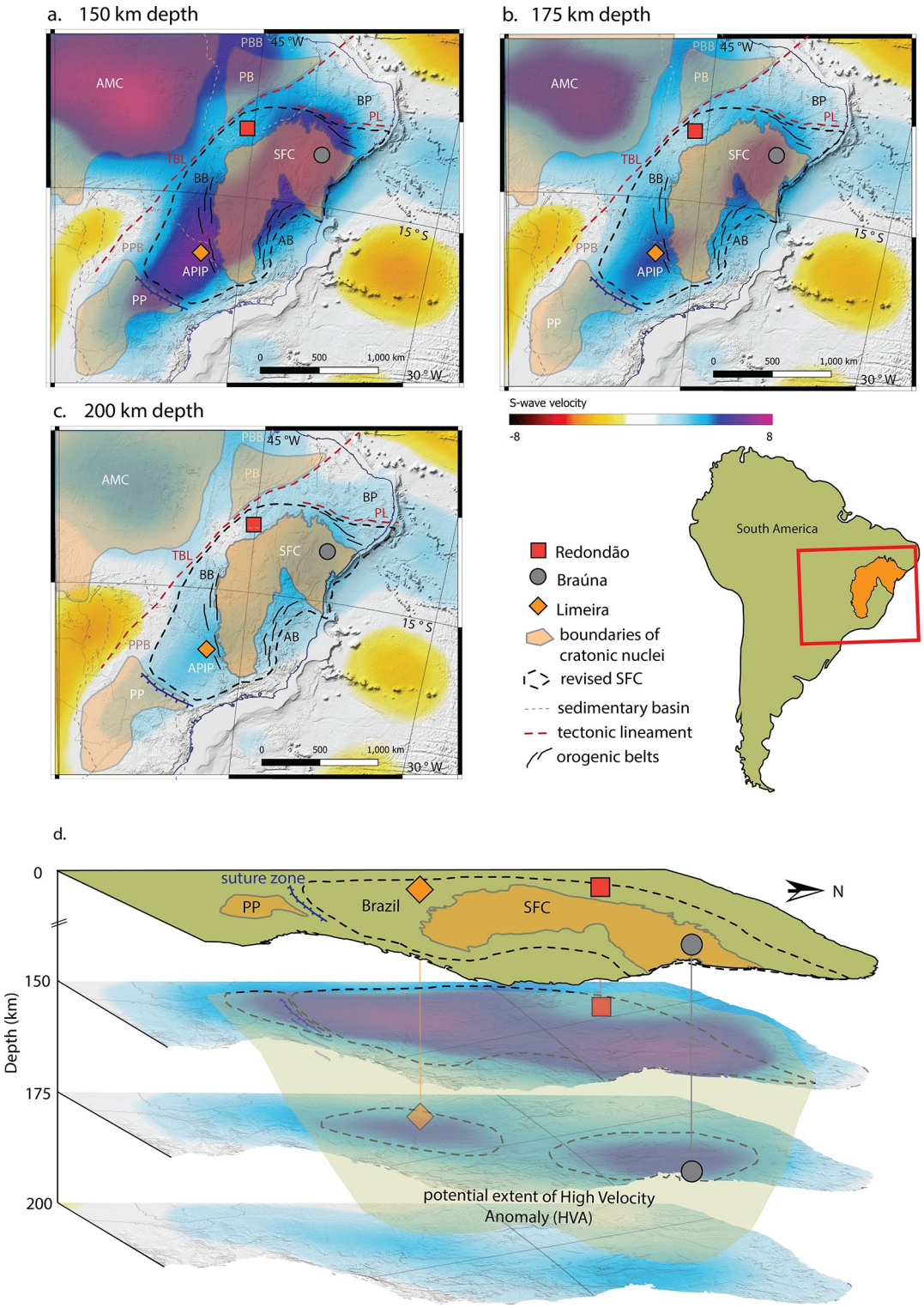

Fig. 9 Tomographic slices through north-eastern Brazil at 150 **(a)**, 175 **(b)** and 200 km depth **(c)** showing S-wave velocities beneath the surface extent of the São Francisco Craton. Depth slices are derived from the S-wave tomographic model from Schaeffer and Lebedev (2013). AMC: Amazonian Craton, TBL: Transbrasiliano Lineament, PL: Pernambuco Lineament (Cordani et al. 2009) BB: Brasilia Belt AB: Araçuaí Belt (Alkmim and Martins-Neto 2012), SFC: São Francisco Craton, PB: Parnaiba Block (de Souza Filho and Seoane 2024), PBB: Parnaiba Basin (de Castro et al. 2016), PP: Paranapanema Block (Affonso et al. 2021), Parana Basin (Osorio and Rodrigues, 2017), APIP: Alto Paranaiba Igneous Province (Fernandes et al. 2021), BP: Borborema Province (de Oliveira et al. 2023). **d)** Proposed extent of the high velocity anomaly beneath the São Francisco Craton

Conclusions

The São Francisco Craton boundaries are commonly defined by the surface expression of ancient Archean age crust and surrounding mobile belts. Recognition of the critical role played by the volumetrically dominant portions of cratons – their mantle lithospheric roots – in stabilising lithospheres through time allows for a more detailed examination of the potential extent of the São Francisco Craton. Petrological and thermobarometric data from peridotites from the Limeira and Redondão kimberlites show that these ancient ultra-refractory peridotite xenoliths were extracted at depths beyond 150 km in classically defined 'off-craton' regions. The combination of petrological and thermobarometric data with geophysical models supports the evidence for the existence of a thick, refractory cratonic root beneath the APIP and Redondão kimberlites to the south-west and north of the canonically defined São Francisco Craton boundaries (Almeida 1977). The proposed revised boundary for the São Francisco Craton encompasses both crustal and subsurface components to define a more accurate representation of the craton area.

Supplementary Information The online version contains supplementary material available at https://doi.org/10.1007/s00710-025-00909-1.

Acknowledgements We owe thanks to Darcy Svisero, deceased, for providing RGA with the Redondão samples. DGP acknowledges a Canada Excellence Research Chairs grant. Analyses were supported by a University of Otago PhD Scholarship to NPC, with additional costs covered by the University of Otago Department of Geology. R. Carlson, E. Thomlinson and K. Smit are thanked for thoroughly reviewing the manuscript.

Funding Open access funding provided by The University of Otago.

References

Affonso G, Rocha M, Costa I, Assumpção M, Fuck R, Albuquerque D, Portner D, Rodríguez E, Beck S (2021) Lithospheric architecture of the Paranapanema block and adjacent nuclei using multiple-frequency P-wave seismic tomography. J Geophys Res: Solid Earth 126:4

Alkmim FF, Marshak S (1998) Transamazonian orogeny in the Southern São Francisco craton region, Minas Gerais, Brazil: evidence for paleoproterozoic collision and collapse in the quadrilátero Ferrıfero. Precambrian Res 90(1–2):29–58

Alkmim FF, Martins-Neto MA (2012) Proterozoic first-order sedimentary sequences of the São Francisco craton, Eastern Brazil. Mar Pet Geol 33(1):127–139

Alkmim FF, Pedrosa-Soares AC, Noce CM, Cruz SCP (2007) Sobre a evolução tectônica do orógeno Araçuaí-Congo ocidental. Geonomos 15(1):25–43

Almeida FFM (1977) O cráton do São Francisco. Rev Bras Geociências 7(4):349–364

Almeida FFM, de Brito Neves BB, Carneiro CDR (2000) The origin and evolution of the South American platform. Earth Sci Rev 50(1–2):77–111

Almeida-Filho R, Castelo Branco RM (1992) Location of kimberlites using LANDSAT thematic mapper images and aerial photographs: the Redondão diatreme, Brazil. Int J Remote Sens 13(8):1449–1457

Artemieva I (2011) The lithosphere: an interdisciplinary approach. Cambridge Univ, p 773

Assumpçao M, An M, Bianchi M, França GS, Rocha M, Barbosa JR, Berrocal J (2004) Seismic studies of the Brasília fold belt at the Western border of the São Francisco craton, central Brazil, using receiver function, surface-wave dispersion and teleseismic tomography. Tectonophysics 388(1–4):173–185

Assumpção M, Azevedo PA, Rocha MP, Bianchi MB (2017) Lithospheric features of the São Francisco Craton: São Francisco craton, Eastern Brazil. In: Heilborn M, Cordani UG, Alkmim FF (eds) São Francisco craton, Eastern Brazil: tectonic genealogy of a miniature continent. Springer, Cham, pp 15–25

Aulbach S, Mungall JE, Pearson DG (2016) Distribution and processing of highly siderophile elements in cratonic mantle lithosphere. Rev Mineral Geochem 81(1):239–304

Azzone RG, Pearson DG, Sarkar C, Chmyz L, Shibata CSV, Luo Y, Ruberti E (2022) Tracking crustal assimilation processes in kimberlites from the Alto Paranaíba igneous Province, Brazil. Petrographic and geochemical controls and the role of perovskites. Lithos 432:106888

Barbosa JSF, Gordilho Barbosa R, Leitzke FP, de Menezes Leal AB, Luciano RL, da Cruz Filho BE, Santana J, de Moraes AMV (2022) A review of the main tectonic settings of Palaeo-and-Mesoarchean ore deposits in the Northern São Francisco craton, NE Brazil. Int Geol Rev 64(21):3121–3132

Barbosa JSF, Sabaté P (2004) Archean and paleoproterozoic crust of the São Francisco craton, Bahia, Brazil: geodynamic features. Precambrian Res 133(1–2):1–27

Barrett N, Jaques AL, González-Álvarez I, Walter MJ, Pearson DG (2022) Ultra-refractory peridotites of phanerozoic mantle origin: the Papua new Guinea ophiolite mantle tectonites. J Petrol 63(3):egac014

Birck JL, Barman MR, Capmas F (1997) Re-Os isotopic measurements at the femtomole level in natural samples. Geostand Newsl 21(1):19–27

Bleeker W (2003) The late archean record: a puzzle in Ca. 35 pieces. Lithos 71(2–4):99–134

Boyd F (1989) Compositional distinction between oceanic and cratonic lithosphere. Earth Planet Sci Lett 96(1–2):15–26

Braga LG, Jalowitzki T, Gervasoni F, Freitas Rodrigues RA, Mazzucchelli M, Giovanardi T, Costa MMD, Santos RV, Rocha MP, Fuck RA (2024) Destruction of the lithosphere beneath the SW margin of the São Francisco craton evidenced by refertilized and deformed mantle xenoliths. J Petrol 65(9):egae087

Brey GP, Köhler T (1990) Geothermobarometry in four-phase lherzolites II. New thermobarometers, and practical assessment of existing thermobarometers. J Petrol 31(6):1353–1378

Campos JCS, Carneiro MA (2008) Neoarchean and paleoproterozoic granitoids marginal to the Jeceaba-Bom sucesso lineament (SE border of the Southern São Francisco craton) genesis and tectonic evolution. J South Am Earth Sci 26(4):463–484

Canil D (1999) The Ni-in-garnet geothermometer: calibration at natural abundances. Contrib Mineral Petrol 136(3):240–246

Carlson RW, Araujo ALN, Junqueira-Brod TC, Gaspar JC, Brod JA, Petrinovic IA, Hollanda MHB, Pimentel MM, Sichel S (2007) Chemical and isotopic relationships between peridotite xenoliths and mafic–ultrapotassic rocks from Southern Brazil. Chem Geol 242(3–4):415–434

Carvalho LD, Jalowitzki T, Scholz R, Gonçalves GO, Rocha MP, Pereira RS, Lana C, de Castro MP, Queiroga G, Fuck RA (2022) An exotic cretaceous kimberlite linked to metasomatized lithospheric mantle beneath the Southwestern margin of the São Francisco craton, Brazil. Geosci Front 13(1):101281

Celli NL, Lebedev S, Schaeffer AJ, Ravenna M, Gaina C (2020) The upper mantle beneath the South Atlantic ocean, South America and Africa from waveform tomography with massive data sets. Geophys J Int 221(1):178–204

Ciardelli C, Assumpção M, Bozdağ E, van der Lee S (2022) Adjoint waveform tomography of South America. J Geophys Res: Solid Earth 127(2):B022575

Coelho FDM, Svisero DP, Felitti Filho W (2010) R15-Geologia e mineralogia da Mina de Diamantes de Romaria, Minas Gerais. Resumos e roteiro de excursão, pp 50–51 https://repositorio.usp.br/directbitstream/41d53bf5-117a-443b-a8b2-a4afd1b3e8e3/2146788.pdf

Cohen AS, Waters FG (1996) Separation of osmium from geological materials by solvent extraction for analysis by thermal ionisation mass spectrometry. Anal Chim Acta 332(2-3):269–75

Coldebella B, Azzone RG, Chmyz L, Ruberti E, Svisero DP (2020) Oxygen fugacity of Alto Paranaíba kimberlites and diamond instability: Três ranchos IV and Limeira I intrusions. Brazilian J Geol 50(1):e20190087

Cooper C, Lenardic A, Levander A, Moresi L, Benn K (2006) Creation and preservation of cratonic lithosphere: seismic constraints and geodynamic models. In: Condie KC, Benn K, Mareschal J-C (eds) Archean geodynamics and environments. Geophys Monograph Ser, vol 164. Wiley Blackwell, pp 75–88

Cordani UG, Brito Neves BBD, Fuck R, Porto R, Thomaz Filho A, Cunha FMB (1984) Estudo preliminar de integração do Pré-Cambriano com os eventos tectônicos das bacias sedimentares brasileiras. Resumos, breves comunicações, cursos, excursões e mesas-redondas, pp 183. https://repositorio.usp.br/directbitstream/78b86d04-138d-4390-af64-18dacac45daf/2951742.pdf

Cordani UG, Teixeira W, D'Agrella-Filho MS, Trindade R (2009) The position of the Amazonian craton in supercontinents. Gondwana Res 15(3–4):396–407

Cordani UG, Teixeira W, Tassinari CC, Coutinho JM, Ruiz AS (2010) The Rio apa craton in Mato Grosso do Sul (Brazil) and Northern Paraguay: geochronological evolution, correlations and tectonic implications for rodinia and Gondwana. Am J Sci 310(9):981–1023

Cruz SCP, Peucat JJ, Teixeira L, Carneiro MA, Martins AAM, dos Santos Santana J, de Souza JS, Barbosa JSF, Leal ÂBM, Dantas E (2012) The Caraguataí syenitic suite, a Ca. 2.7 Ga-old alkaline magmatism (petrology, geochemistry and U–Pb Zircon ages). Southern Gavião block (São Francisco Craton), Brazil. J South Am Earth Sci 37:95–112

de Azevedo PA, Rocha MP, Soares JEP, Fuck RA (2015) Thin lithosphere between the Amazonian and São Francisco cratons, in central Brazil, revealed by seismic P-wave tomography. Geophys J Int 201(1):61–69

de Castro DL, Bezerra FH, Fuck RA, Vidotti RM (2016) Geophysical evidence of pre-sag rifting and post-rifting fault reactivation in the Parnaíba basin, Brazil. Solid Earth 7(2):529–548

de Morisson Valeriano C, Mendes JC, Tupinambá M, Bongiolo E, Heilbron M, Junho MCB (2016) Cambro-Ordovician post-collisional granites of the Ribeira belt, SE-Brazil: a case of terminal magmatism of a hot orogen. J South Am Earth Sci 68:269–281

de Oliveira RG, de Medeiros WE, Domingos NRR, Rodrigues MAC (2023) A review of the geophysical knowledge of the Borborema Province, NE-Brazil, and tectonic implications. J South Am Earth Sci 126:104360

de Sousa DM, Oliveira E, Amaral W, Baldim M (2020) The Itabuna-Salvador-Curaçá orogen revisited, São Francisco craton, Brazil: new Zircon U–Pb ages and hf data support evolution from Archean continental Arc to paleoproterozoic crustal reworking during block collision. J South Am Earth Sci 104:102826

de Souza Filho RG, Seoane JCS (2022) Defining lithospheric limits with deep sourced geophysics: the case of São Francisco craton and Borborema Province. Brazilian J Geophys 40(4). https://doi.org/10.22564/brjg.v40i4.2184

de Souza Filho RG, Seoane JCS (2024) Neoproterozoic lithospheric structures at the Borborema Province: integration of magnetotelluric resistivity sections and their relations to neighboring lithospheric blocks of the Parnaíba basin and São Francisco craton. J South Am Earth Sci 138:104879

de Wit MJ, de Ronde CE, Tredoux M, Roering C, Hart RJ, Armstrong RA, Green RW, Peberdy E, Hart RA (1992) Formation of an Archaean continent. Nature 357(6379):553–562

Donatti-Filho J, Oliveira E, McNaughton N (2010) Age constraints for the Serrinha block lithosphere based on inherited zircons from the neoproterozoic Brauna kimberlite field, São Francisco craton, Bahia, Brazil. Abstracts of the 45 Congr Brasil Geol, Belém, Brazil

Donatti Filho J, Oliveira E, Pisani J, Ochika F (2008) Geochemistry and mineralogy of kimberlites from the Braúna kimberlite province, São Francisco Craton, NE Brazil. Proceedings International Kimberlite Conference: Extended Abstracts 9

Donatti-Filho JP, Tappe S, Oliveira EP, Heaman LM (2013) Age and origin of the neoproterozoic Brauna kimberlites: melt generation within the metasomatized base of the São Francisco craton, Brazil. Chem Geol 353:19–35

Engler A, Koller F, Meisel T, Quéméneur J (2002) Evolution of the archean/proterozoic crust in the Southern São Francisco craton near Perdões, Minas Gerais, Brazil: petrological and geochemical constraints. J South Am Earth Sci 15(6):709–723

Farina F, Albert C, Lana C (2015) The neoarchean transition between medium-and high-K granitoids: clues from the Southern São Francisco craton (Brazil). Precambrian Res 266:375–394

Fernandes PR, Tommasi A, Vauchez A, Neves SP, Nannini F (2021) The São Francisco cratonic root beneath the neoproterozoic Brasilia belt (Brazil): petrophysical data from kimberlite xenoliths. Tectonophysics 816:229011

Frederiksen A, Bostock M, Cassidy J (2001) S-wave velocity structure of the Canadian upper mantle. Phys Earth Planet Inter 124(3–4):175–191

Ganade CE, Weinberg RF, Caxito FA, Lopes LB, Tesser LR, Costa IS (2021) Decratonization by rifting enables orogenic reworking and transcurrent dispersal of old terranes in NE Brazil. Sci Rep 11(1):5719

Ganade de Araujo CE, Weinberg RF, Cordani UG (2014) Extruding the Borborema Province (NE-Brazil): a two-stage neoproterozoic collision process. Terra Nova 26(2):157–168

Goulart LEA, Carneiro MA, Endo I, Suita MTF (2013) New evidence of neoarchean crustal growth in Southern São Francisco Craton:

the carmópolis de Minas layered suite, Minas Gerais, Brazil. Braz J Geol 43(3):445–459
Griffin W, Fisher N, Friedman J, O'Reilly SY, Ryan C (2002) Cr-pyrope garnets in the lithospheric mantle 2. Compositional populations and their distribution in time and space. Geochem Geophys Geosyst 3(12):1–35
Griffin W, Fisher N, Friedman J, Ryan C, O'Reilly S (1999) Cr-pyrope garnets in the lithospheric mantle. I. Compositional systematics and relations to tectonic setting. J Petrol 40(5):679–704
Griffin W, O'Reilly S, Abe N, Aulbach S, Davies R, Pearson N, Doyle B, Kivi K (2003) The origin and evolution of archean lithospheric mantle. Precambrian Res 127(1–3):19–41
Grütter HS, Gurney JJ, Menzies AH, Winter F (2004) An updated classification scheme for mantle-derived Garnet, for use by diamond explorers. Lithos 77(1–4):841–857
Guarino V, Bonazzi M, Nimis P, Azzone RG, Cariddi B, Zanetti A (2024) Stabilization and evolution of the Brazilian Subcontinental lithospheric mantle: insights from Garnet xenocrysts and peridotite xenoliths of Três ranchos kimberlite (APIP, Brazil). Gondwana Res 130:18–35
Guarino V, Wu F-Y, Lustrino M, Melluso L, Brotzu P, de Barros Gomes C, Ruberti E, Tassinari CCG, Svisero DP (2013) U–Pb ages, Sr–Nd-isotope geochemistry, and petrogenesis of kimberlites, Kamafugites and phlogopite-picrites of the Alto Paranaíba igneous Province, Brazil. Chem Geol 353:65–82
Guimães JT, Alkmim FF, Cruz SCP (2012) Supergrupos Espinhaço e São Francisco. In: Barbosa JSF, Mascarenhas J, Correa Gomes L, Dominguez L, de Santos J (eds) Geologia Da Bahia: pesquisa e atualização. Companhia Baiana de Pesquisa Mineral, Salvador, pp 33–85
Hartmann LA, Campal N, Santos JOS, McNaughton NJ, Bossi J, Schipilov A, Lafon J-M (2001) Archean crust in the Rio de La Plata craton, Uruguay—SHRIMP U–Pb Zircon reconnaissance geochronology. J South Am Earth Sci 14(6):557–570
Hasterok D, Chapman D (2011) Heat production and geotherms for the continental lithosphere. Earth Planet Sci Lett 307(1–2):59–70
Hasui Y (2012) Sistema Orogênico Borborema, in Y Hasui, CDR Carneiro, FFM Almeida, and A Bartorelli, orgs., Geologia do Brasil: Beca Editora, São Paulo, Brazil, pp 254–288
Heilbron M, Cordani UG, Alkmim FF, Reis HL (2017) Tectonic genealogy of a miniature continent. In: Heilborn M, Cordani UG, Alkmim FF (eds) São Francisco craton, Eastern Brazil: tectonic genealogy of a miniature continent. Springer, Cham, pp 321–331
Heller BM, Hueck M, Passarelli CR, Basei MA (2021) Zircon U-Pb geochronology and hf isotopes of the Luís Alves Terrane: archean to paleoproterozoic evolution and neoproterozoic overprint. J South Am Earth Sci 106:103008
Herzberg C, Rudnick R (2012) Formation of cratonic lithosphere: an integrated thermal and petrological model. Lithos 149:4–15
Jarosewich E, Nelen J, Norberg JA (1980) Reference samples for electron microprobe analysis. Geostand Newslett 4(1):43–47
Jochum KP, Stoll B (2008) Reference materials for elemental and isotopic analyses by LA-(MC)-ICP-MS: successes and outstanding needs. Min Assoc Can Short Course Ser 40:Qu–becQCpp147
Jochum KP, Willbold M, Raczek I, Stoll B, Herwig K (2005) Chemical characterisation of the USGS reference glasses GSA-1G, GSC-1G, GSD-1G, GSE-1G, BCR-2G, BHVO-2G and BIR-1G using EPMA, ID-TIMS, ID-ICP-MS and LA-ICP-MS. Geostand Geoanal Resarch 29(3):285–302
Kaminsky FV, Sablukov SM, Sablukova LI, Zakharchenko OD (2009) The Fazenda Largo off-craton kimberlites of Piauí State, Brazil. J South Am Earth Sci 28(3):288–303
Kaminsky F, Zakharchenko O, Davies R, Griffin W, Khachatryan-Blinova G, Shiryaev A (2001) Superdeep diamonds from the Juina area, Mato Grosso State, Brazil. Contrib Mineral Petrol 140:734–753
Klein EL, Lucas FR, Queiroz JD, Freitas SC, Renac C, Galarza MA, Jourdan F, Armstrong R (2015) Metallogenesis of the paleoproterozoic Piaba orogenic gold deposit, São Luís cratonic fragment, Brazil. Ore Geol Rev 65:1–25
Klemme S (2004) The influence of cr on the garnet–spinel transition in the Earth's mantle: experiments in the system MgO–Cr2O3–SiO2 and thermodynamic modelling. Lithos 77(1–4):639–646
Kuchenbecker M, Reis HLS, da Silva LC, da Costa RD, Fragoso DGC, Knauer LG, Dussin IA, Soares ACP (2015) Age constraints for deposition and sedimentary provenance of Espinhaço supergroup and Bambuí group in Eastern São Francisco craton. Rev Geonomos 23(2):14–28
Lana C, Alkmim FF, Armstrong R, Scholz R, Romano R, Nalini HA Jr (2013) The ancestry and magmatic evolution of Archaean TTG rocks of the quadrilátero Ferrífero Province, Southeast Brazil. Precambrian Res 231:157–173
Leal LRB, Cunha JC, Cordani UG, Teixeira W, Nutman AP, Leal ABM, Macambira MJ (2003) SHRIMP U–Pb, 207Pb/206Pb Zircon dating, and Nd isotopic signature of the umburanas greenstone belt, Northern São Francisco craton, Brazil. J South Am Earth Sci 15(7):775–785
Lopes LBL, Ganade CE, Campos LD, Rodrigues JB, de Oliveira LBT, Larizzatti JH, Shen M, Gao T, Xu M, Zhou Y (2021) Crustal reworking and archean TTG generation in the South Gavião block, São Francisco craton, Brazil. Precambrian Res 363:106333
Luguet A, Nowell GM, Pearson DG (2008) 186Os measurements by N-TIMS: Effects of interfering element and mass fractionation correction on data accuracy and precision. Chem Geol 248
Machado N, Noce C, Ladeira E, De Oliveira OB (1992) U-Pb geochronology of archean magmatism and proterozoic metamorphism in the quadrilátero Ferrífero, Southern São Francisco craton, Brazil. Geol Soc Am Bull 104(9):1221–1227
Mantovani MSM, de Brito Neves B (2005) The Paranapanema lithospheric block: its importance for proterozoic (Rodinia, Gondwana) supercontinent theories. Gondwana Res 8(3):303–315
Marinho M, Barbosa JS, Vidal P (1993) The basement from São Francisco Craton in Bahia southeastern: Geochronological review. O embasamento do craton do Sao Francisco no sudeste da Bahia: Revisao geocronologica. 2nd Symp on Sao Francisco Craton: tectonic and metallogenetic evolution from Sao Francisco craton. Salvador, Brazil. CONF-9308252, pp 1–5
Marinho MM (1991) La sequence volcano-sedimentaire de contendas-mirante et la bordure occidentale du bloc de jequie (craton du sao francisco, bresil): Un exemple de transition archeen-proterozoique. PhD thesis, Univ Clermont-Ferrand 2
Martin H, Peucat J, Sabaté P, Cunha J (1997) Crustal evolution in the early Archaean of South America: example of the Sete Voltas Massif, Bahia State, Brazil. Precambrian Res 82(1–2):35–62
Martins PLG, Toledo CLB, Silva AM, Chemale F Jr, Santos JOS, Assis LM (2017) Neoarchean magmatism in the southeastern Amazonian craton, Brazil: petrography, geochemistry and tectonic significance of basalts from the Carajás basin. Precambrian Res 302:340–357
McDonough WF, Sun SS (1995) The composition of the Earth. Chem Geol 120(3-4):223–53
Meisel T, Walker RJ, Irving AJ, Lorand J-P (2001) Osmium isotopic compositions of mantle xenoliths: A global perspective. Geochim Cosmochim Acta 65(8):1311–1323
Milani EJ, Ramos VA (1998) Orogenias paleozóicas no Domínio sul-ocidental do Gondwana e Os Ciclos de subsidência Da Bacia do Paraná. Rev Bras Geociências 28(4):473–484
Moreira H, Schannor M, Cutts K, Roberts NM (2022) The dynamic archean to paleoproterozoic crustal evolution of Brazil: preface. Geosci Front 13:101406
Mundl A, Ntaflos T, Ackerman L, Bizimis M, Bjerg EA, Wegner W, Hauzenberger C (2016) Geochemical and Os–Hf–Nd–Sr isotopic

characterization of North Patagonian mantle xenoliths: implications for extensive melt extraction and percolation processes. J Petrol 57(4):685–715

Neves SP (2021) Comparative geological evolution of the Borborema Province and São Francisco craton (eastern Brazil): decratonization and crustal reworking during West Gondwana assembly and implications for paleogeographic reconstructions. Precambrian Res 355:106119

Ngonge ED, de Hollanda MHBM, Puchtel IS, Walker RJ, Archanjo CJ (2019) Characteristics of the lithospheric mantle beneath Northeastern Borborema Province, Brazil: Re–Os and HSE constraints on peridotite xenoliths. J South Am Earth Sci 96:102371

Nimis P, Taylor WR (2000) Single clinopyroxene thermobarometry for Garnet peridotites. Part I. Calibration and testing of a Cr-in-Cpx barometer and an enstatite-in-Cpx thermometer. Contrib Mineral Petrol 139:541–554

Noce CM, Tassinari C, Lobato LM (2007) Geochronological framework of the quadrilátero Ferrífero, with emphasis on the age of gold mineralization hosted in archean greenstone belts. Ore Geol Rev 32(3–4):500–510

Nutman A, Cordani UG, Sabaté P (1994) SHRIMP U-Pb ages of detrital zircons from the early proterozoic Contendas-Mirante supracrustal belt, São Francisco craton, Bahia, Brazil. J South Am Earth Sci 7(2):109–114

Oliveira EP, McNaughton NJ, Zincone SA, Talavera C (2020) Birthplace of the São Francisco craton, Brazil: evidence from 3.60 to 3.64 Ga gneisses of the Mairi gneiss complex. Terra Nova 32(4):281–289

Osorio LL, Dos Reis DE, Rodrigues R (2017) Aromatic steroids biomarkers applied to high resolution stratigraphy: Irati formation, Southern of Paraná basin, Brazil. J Sedim Envi 2:274–282

Oyhantçabal P, Oriolo S, Philipp RP, Wemmer K, Siegesmund S (2018) The Nico Pérez terrane of Uruguay and southeastern Brazil. In: Siegesmund S, Basei MAS, Oyhantçabal P, Oriolo S (eds) (esd) Geology of Southwest Gondwana. Springer, Cham, pp 161–188

Paton C, Hellstrom J, Paul B, Woodhead J, Hergt J (2011) Iolite: freeware for the visualisation and processing of mass spectrometric data. J Anal At Spectrom (12):2508–18

Pearson DG, Scott JM, Liu J, Schaeffer A, Wang LH, van Hunen J, Szilas K, Chacko T, Kelemen PB (2021) Deep continental roots and cratons. Nature 596(7871):199–210

Pereira RS, de Carvalho LDV, Fuck RA (2021) Primary source of alluvial diamonds from the Santo Antônio do Bonito, Santo Inácio, and Douradinho rivers, Coromandel region, Minas Gerais, Brazil. J South Am Earth Sci 111:103461

Pereira RS, Fuck RA (2005) Archean nucleii and the distribution of kimberlite and related rocks in the São Francisco craton, Brazil. Rev Bras Geociências 35(3):93–104

Pisani S, Timm JR, Tainton KM, Allan AF, Silva SB, Iranda JV (2001) Geology and exploration of the Brauna diamondiferous kimberlites, Serrinha block, Bahia, Brazil. Rev Bras Geociências 31:663

Polet J, Anderson DL (1995) Depth extent of cratons as inferred from tomographic studies. Geology 23(3):205–208

Rocha MP, Azevedo PAd, Assumpção M, Pedrosa-Soares AC, Fuck R, Von Huelsen MG (2019a) Delimiting the neoproterozoic São Francisco Paleocontinental block with P-wave traveltime tomography. Geophys J Int 219(1):633–644

Rocha MP, Schimmel M, Assumpção M (2011) Upper-mantle seismic structure beneath SE and central Brazil from P-and S-wave regional traveltime tomography. Geophys J Int 184(1):268–286

Rocha NS, Fontes SL, La Terra EF, Fuck RA (2019b) Lithosphere structures of the Parnaíba basin and adjacent provinces revealed by deep magnetotelluric imaging. J South Am Earth Sci 92:1–11

Romano R, Lana C, Alkmim FF, Stevens G, Armstrong R (2013) Stabilization of the Southern portion of the São Francisco craton, SE Brazil, through a long-lived period of Potassic magmatism. Precambrian Res 224:143–159

Ryan CG, Griffin WL, Pearson NJ (1996) Garnet geotherms: Pressure-temperature data from Cr-pyrope Garnet xenocrysts in volcanic rocks. J Geophys Res: Solid Earth 101(B3):5611–5625

Santos AC, Padilha AL, Fuck RA, Pires AC, Vitorello I, Padua MB (2014) Deep structure of a stretched lithosphere: magnetotelluric imaging of the southeastern Borborema Province, NE Brazil. Tectonophysics 610:39–50

Santos LCML, Lima HM, Lages GA, Caxito FA, Araújo JF, Guimarães IP (2020) Petrogenesis of the Riacho do Icó stock: evidence for neoproterozoic slab melting during accretion tectonics in the Borborema Province? Brazilian J Geol 50(2):e20190127

Santos-Pinto M, Peucat JJ, Martin H, Barbosa JS, Fanning CM, Cocherie A, Paquette JL (2012) Crustal evolution between 2.0 and 3.5 Ga in the Southern Gavião block (Umburanas-Brumado-Aracatu region), São Francisco craton, Brazil: A 3.5–3.8 Ga proto-crust in the Gavião block? J South Am Earth Sci 40:129–142

Schaeffer A, Lebedev S (2013) Global shear speed structure of the upper mantle and transition zone. Geophys J Int 194(1):417–449

Schilling ME, Carlson RW, Conceição RV, Dantas C, Bertotto GW, Koester E (2008) Re–Os isotope constraints on Subcontinental lithospheric mantle evolution of Southern South America. Earth Planet Sci Lett 268(1–2):89–101

Schilling ME, Carlson RW, Tassara A, Conceição RV, Bertotto GW, Vásquez M, Muñoz D, Jalowitzki T, Gervasoni F, Morata D (2017) The origin of patagonia revealed by Re-Os systematics of mantle xenoliths. Precambrian Res 294:15–32

Scott JM (2020) An updated catalogue of New Zealand's mantle peridotite and serpentinite. N Z J Geol Geophys 63(4):428–49

Smith AG, Hallam A (1970) The fit of the Southern continents. Nature 225(5228)

Smith CB, Pearson DG, Bulanova GP, Beard AD, Carlson RW, Wittig N, Sims K, Chimuka L, Muchemwa E (2009) Extremely depleted lithospheric mantle and diamonds beneath the Southern Zimbabwe craton. Lithos 112:1120–1132

Sudholz Z, Green D, Yaxley G, Jaques AL (2022) Mantle geothermometry: experimental evaluation and recalibration of Fe–Mg geothermometers for garnet-clinopyroxene and garnet-orthopyroxene in peridotite, pyroxenite and eclogite systems. Contrib Mineral Petrol 177(8):77

Sudholz ZJ, Yaxley GM, Jaques AL, Brey GP (2021a) Experimental recalibration of the Cr-in-clinopyroxene geobarometer: improved precision and reliability above 4.5 GPa. Contrib Mineral Petrol 176:1–20

Sudholz ZJ, Yaxley GM, Jaques AL, Chen J (2021b) Ni-in-garnet geothermometry in mantle rocks: a high pressure experimental recalibration between 1100 and 1325° C. Contrib Min Petrol 176:1–16

Svisero DP (1995) Distribution and origin of diamonds in Brazil: an overview. J Geodyn 20(4):493–514

Svisero DP, Meyer HO, Tsai H-M (1977) Kimberlite minerals from vargem (Minas Gerais) and Redondão (Piauí) diatremes, Brazil: and Garnet lherzolite xenolith from Redondão diatreme. Rev Bras Geociências 7(1):1–13

Svisero DP, Meyers HO, Haralyp N, Hasui Y (1982) Geology of Brazilian kimberlites. In: Proceedings International Kimberlite Conference: Extended Abstracts, vol 3, pp 246–247

Teixeira CD, Chemale F, Von Huelsen MG (2021) Integrated geophysics analysis of crustal structure in the NE Pirapora aulacogen, Brazil. J South Am Earth Sci 112:103585

Teixeira W, Oliveira EP, Marques LS (2017) Nature and evolution of the archean crust of the São Francisco craton. In: Heilborn M, Cordani UG, Alkmim FF (eds) São Francisco craton, Eastern Brazil: tectonic genealogy of a miniature continent. Springer, Cham, pp 29–56

Teixeira W, Sabaté P, Barbosa J, Noce C, Carneiro M (2000) Archean and Paleoproterozoic tectonic evolution of the São Francisco craton, Brazil. In: Cordani UG, Milani EJ, Thomaz Filho A, Campos AD (eds) Tectonic Evolution of South America. 31st Int Geol Congress, Rio de Janeiro, pp 1–64

Terentiev R, Santosh M (2020) Baltica (East European Craton) and Atlantica (Amazonian and West African Cratons) in the proterozoic: the pre-Columbia connection. Earth-Sci Rev 210:103378

Vandenburg ED, Nebel O, Cawood PA, Smithies RH, Capitanio FA, Miller LA, Millet M-A, Bruand E, Moyen J-F, Wang X (2023) The stability of cratons is controlled by lithospheric thickness, as evidenced by Rb-Sr overprint ages in granitoids. Earth Planet Sci Lett 621:118401

Walker RJ, Carlson RW, Shirey SB, Boyd FR (1989) Os, Sr, Nd, and Pb isotope systematics of Southern African peridotite xenoliths: implications for the chemical evolution of Subcontinental mantle. Geochim Cosmochim Acta 53(7):1583–1595

Wittig N, Webb M, Pearson D, Dale C, Ottley C, Hutchison M, Jensen S, Luguet A (2010) Formation of the North Atlantic Craton: timing and mechanisms constrained from Re–Os isotope and PGE data of peridotite xenoliths from SW Greenland. Chem Geol 276(3–4):166–187